A *Spitzer* high-resolution mid-infrared spectral atlas of starburst galaxies

The Astrophysical Journal Supplement Series, 184:230–247, 2009 October doi:10.1088/0067-0049/184/2/230

A *SPITZER* HIGH-RESOLUTION MID-INFRARED SPECTRAL ATLAS OF STARBURST GALAXIES

J. Bernard-Salas[1], H. W. W. Spoon[1], V. Charmandaris[2,3,4], V. Lebouteiller[1], D. Farrah[1,5], D. Devost[6], B. R. Brandl[7], Yanling Wu[1,8], L. Armus[8], L. Hao[1,9], G. C. Sloan[1], D. Weedman[1], and J. R. Houck[1]
[1] Cornell University, 222 Space Sciences Bld., Ithaca, NY 14853, USA
[2] Department of Physics, University of Crete, GR-71003, Heraklion, Greece
[3] IESL/Foundation for Research & Technology-Hellas, GR-71110, Heraklion, Greece
[4] Chercheur Associé, Observatoire de Paris, F-75014, Paris, France
[5] Department of Physics and Astronomy, University of Sussex, Brighton, East Sussex BN1 9QH, UK
[6] CFHT Corporation, 65-1238 Mamalahoa Hwy, Kamuela, HI 96743, USA
[7] Leiden Observatory, Leiden University, P.O. Box 9513, 2300 RA Leiden, The Netherlands
[8] *Spitzer* Science Center, MS 220-06, California Institute of Technology, Pasadena, CA 91125, USA
[9] Department of Astronomy, University of Texas at Austin, Austin, TX 78712-0259, USA
Received 2009 March 6; accepted 2009 August 14; published 2009 September 16

ABSTRACT

We present an atlas of *Spitzer*/IRS high-resolution ($R \sim 600$) 10–37 μm spectra for 24 well known starburst galaxies. The spectra are dominated by fine-structure lines, molecular hydrogen lines, and emission bands of polycyclic aromatic hydrocarbons (PAHs). Six out of the eight objects with a known active galactic nucleus (AGN) component show emission of the high excitation [Ne v] line. This line is also seen in one other object (NGC 4194) with, a priori, no known AGN component. In addition to strong PAH emission features in this wavelength range (11.3, 12.7, 16.4 μm), the spectra reveal other weak hydrocarbon features at 10.6, 13.5, 14.2 μm, and a previously unreported emission feature at 10.75 μm. An unidentified absorption feature at 13.7 μm is detected in many of the starbursts. We use the fine-structure lines to derive the abundance of neon and sulfur for 14 objects where the H I 7-6 line is detected. We further use the molecular hydrogen lines to sample the properties of the warm molecular gas. Several basic diagrams characterizing the properties of the sample are also shown. We have combined the spectra of all the pure starburst objects to create a high signal-to-noise ratio template, which is available to the community.

Key words: galaxies: starburst – infrared: galaxies – ISM: lines and bands

Online-only material: supplementary data file

1. INTRODUCTION

As galaxies evolve, they often go through periods when their star formation rates increase substantially. This is usually ascribed to large-scale perturbations in their structure, such as the formation of bars triggered by interactions with companions, leading to the accumulation of large quantities of gas in their nuclei. A small number of those so-called "starburst" galaxies (e.g., Weedman et al. 1981) have been identified in the local universe and have been studied extensively at all wavelengths. At high redshifts, obscured starburst galaxies are much more common (Blain et al. 2002; Elbaz & Cesarsky 2003), and are believed to give rise to the bulk of the cosmic infrared background radiation. Reviews of their properties can be found in Kennicutt (1998), Lagache et al. (2005), and Lonsdale et al. (2006).

Understanding the physics of starburst galaxies in the local universe is of great importance, as they are the closest laboratories we have for studying the starburst phenomenon, and because they may represent "scaled-down" versions of the starbursts seen at high redshift. The obscured nature of (most) starburst galaxies, regardless of their redshifts, however means that probing their nuclear regions in the optical is challenging. This task is better done in the infrared, where dust opacity is lower. The advent of major infrared space facilities such as *IRAS* (Neugebauer et al. 1984), *Infrared Space Observatory* (*ISO*; Kessler et al. 1996), and *Spitzer* (Werner et al. 2004), and in particular the accessibility to high quality spectroscopy has allowed great progress in this field, including detailed studies of the mid-infrared (MIR) region of the spectrum in galaxies. It was discovered that the MIR is rich in emission and absorption features of gas and dust. Emission from polycyclic aromatic hydrocarbons (PAHs; Leger & Puget 1984) was shown to be a reliable star formation tracer (e.g., Roussel et al. 2001; Förster Schreiber et al. 2004; Peeters et al. 2004), though variations with metallicity have also been observed (Wu et al. 2006; Smith et al. 2007; Rosenberg et al. 2008). The use of infrared atomic lines with different degrees of ionization has proven invaluable in studying the properties of the ionization field in starbursts (e.g., Sturm et al. 2002; Verma et al. 2003; Wu et al. 2006; Dale et al. 2006). In ultra-luminous infrared galaxies (ULIRGs), diagnostic diagrams based on line ratios such as [Ne vλ14.32 μm]/[Ne IIλ12.81 μm], [O IV λ25.89 μm]/[Ne IIλ12.81 μm], [S IIIλ33.48 μm]/[Si II λ 34.82 μm], and combinations of those with PAH emission features have been developed to reveal their nature (e.g., Genzel et al. 1998; Laurent et al. 2000; Thornley et al. 2000; Dale et al. 2006; Armus et al. 2007; Farrah et al. 2007, 2008). Additional diagnostics using the silicate absorption features (Spoon et al. 2007) or the strength of the rotational molecular hydrogen lines (e.g., Rigopoulou et al. 1999; Roussel et al. 2007) have also been proposed.

As part of our continuing efforts to provide a comprehensive picture of the starburst phenomenon at low redshifts, we here present an atlas of high-resolution ($R \sim 600$) 9.7–37 μm spectra of well known nearby starburst galaxies, taken with the Infrared Spectrograph[10] (Houck et al. 2004) on-board *Spitzer*.

[10] The *IRS* was a collaborative venture between Cornell University and Ball Aerospace Corporation funded by NASA through the Jet Propulsion Laboratory and the Ames Research Center.

Table 1
The Starburst Galaxy Sample

Name	Type	R.A.	Decl.	z	D (Mpc)	log[L_{IR}] ($L_\odot$)	AOR ID[a]	SH t_{int} (cycles ×s)	LH t_{int} (cycles × s)
NGC 253	SB	$00^h47^m33\overset{s}{.}12$	$-25^d17^m17\overset{s}{.}6$	0.0008	2.5	10.23	9072640	12 × 6	12 × 6
NGC 520	SB	$01^h24^m35\overset{s}{.}07$	$+03^d47^m32\overset{s}{.}7$	0.0076	30.2	10.91	9073408	4 × 30	3 × 60
NGC 660	SB+AGN[b]	$01^h43^m02\overset{s}{.}35$	$+13^d38^m44\overset{s}{.}4$	0.00283	12.3	10.49	9070848	4 × 30	8 × 14
NGC 1097	SB+AGN[b]	$02^h46^m19\overset{s}{.}08$	$-30^d16^m28\overset{s}{.}0$	0.00456	16.8	10.71	3758080	4 × 30	2 × 60
NGC 1222	SB	$03^h08^m56\overset{s}{.}74$	$-02^d57^m18\overset{s}{.}5$	0.00818	32.3	10.60	9071872	4 × 30	2 × 60
NGC 1365	SB+AGN[b]	$03^h33^m36\overset{s}{.}37$	$-36^d08^m25\overset{s}{.}5$	0.00545	17.9	11.00	8767232	4 × 30	8 × 14
IC 342	SB	$03^h46^m48\overset{s}{.}51$	$+68^d05^m46\overset{s}{.}0$	0.00010	4.6	10.17	9072128	4 × 30	8 × 14
NGC 1614	SB	$04^h33^m59\overset{s}{.}85$	$-08^d34^m44\overset{s}{.}0$	0.016	62.6	11.60	3757056	4 × 30	8 × 14
NGC 2146	SB	$06^h18^m37\overset{s}{.}71$	$+78^d21^m25\overset{s}{.}3$	0.003	16.5	11.07	9074432	1 × 6	1 × 60
NGC 2623	SB+AGN[b]	$08^h38^m24\overset{s}{.}08$	$+25^d45^m16\overset{s}{.}9$	0.01846	77.4	11.54	9072896	4 × 30	2 × 60
NGC 3079	SB+AGN[b]	$10^h01^m57\overset{s}{.}80$	$+55^d40^m47\overset{s}{.}1$	0.00372	17.6	10.52	3755520	4 × 30	2 × 60
NGC 3256	SB	$10^h27^m51\overset{s}{.}27$	$-43^d54^m13\overset{s}{.}8$	0.00913	35.4	11.56	9073920	1 × 6	1 × 60
NGC 3310	SB	$10^h38^m45\overset{s}{.}96$	$+53^d30^m05\overset{s}{.}3$	0.0033	19.8	10.61	9071616	4 × 30	2 × 60
NGC 3556	SB	$11^h11^m30\overset{s}{.}97$	$+55^d40^m26\overset{s}{.}8$	0.00233	13.9	10.37	9070592	4 × 30	2 × 60
NGC 3628	SB+AGN[b]	$11^h20^m17\overset{s}{.}02$	$+13^d35^m22\overset{s}{.}2$	0.00281	10.0	10.25	9070080	4 × 30	2 × 60
NGC 4088	SB	$12^h05^m34\overset{s}{.}19$	$+50^d32^m20\overset{s}{.}5$	0.00252	13.4	10.25	9070336	4 × 30	2 × 60
NGC 4194	SB+AGN[c]	$12^h14^m09\overset{s}{.}64$	$+54^d31^m34\overset{s}{.}6$	0.00835	40.3	11.06	3757824	4 × 30	2 × 60
Mrk 52	SB	$12^h25^m42\overset{s}{.}67$	$+00^d34^m20\overset{s}{.}4$	0.0071	30.1	10.14	3753216	4 × 30	2 × 60
NGC 4676	SB	$12^h46^m10\overset{s}{.}10$	$+30^d43^m55\overset{s}{.}0$	0.022	94.0	10.88	9073152	8 × 30	6 × 60
NGC 4818	SB	$12^h56^m48\overset{s}{.}90$	$-08^d31^m31\overset{s}{.}1$	0.00355	9.4	09.75	9071104	4 × 30	2 × 60
NGC 4945	SB+AGN[b]	$13^h05^m27\overset{s}{.}48$	$-49^d28^m05\overset{s}{.}6$	0.00186	3.9	10.48	8769280	1 × 6	1 × 60
Mrk 266	SB+AGN[b]	$13^h38^m17\overset{s}{.}69$	$+48^d16^m33\overset{s}{.}9$	0.02786	115.8	11.49	3755264[d]	4 × 30	2 × 60
NGC 7252	SB	$22^h20^m44\overset{s}{.}77$	$-24^d40^m41\overset{s}{.}8$	0.0156	66.4	10.75	9074688	4 × 30	3 × 60
NGC 7714	SB	$23^h36^m14\overset{s}{.}10$	$+02^d09^m18\overset{s}{.}6$	0.00933	38.2	10.72	3756800	4 × 30	2 × 60

Notes.
[a] This is the AOR ID of the high-resolution observations only.
[b] The evidence for an AGN in these objects come from the literature (NED).
[c] The evidence for an AGN comes from the detection of the [Ne v] line in this work.
[d] The coordinates in the table for this galaxy are slightly off the nucleus (see Section 2 and Figure 1). The galaxy is still included in the LH slit but for the smaller SH slit we used an observation from a different program (PID = 3237, AORkey = 10510592) where the source is well centered.

This follows on from our earlier work on the same sample using the low-resolution IRS modules (Brandl et al. 2006). We have created a high signal-to-noise ratio (S/N) template from these spectra. Our goal is to make this set of high quality spectra available to the community, and to report on their characteristic features. Observations are described in Section 2, and data reduction and analysis is described in Section 3. We present results in Section 4 and discussion in Section 5. Finally, we summarize our conclusions in Section 6.

2. OBSERVATIONS

Our sample is presented in Table 1 where information on the galaxy optical classifications, distances, magnitudes, and other basic information on the observations is given. In nine objects there is evidence of an active galactic nucleus (AGN), even though it does not dominate the bolometric luminosity of the system. The sample was observed as part of the IRS Guaranteed Time program (PID 14) and consists of 24 well known nearby starburst galaxies, with an average distance of 33 Mpc and an average infrared (IR; 8–1000 μm) luminosity of $5\times10^{10}L_\odot$. The observations were made using both the high- and low-resolution modules of the IRS. Here we present the high-resolution spectra. The low-resolution spectra can be found in the companion paper by Brandl et al. (2006).

The two high-resolution modules, short-high (SH) and long-high (LH), cover the wavelength region between 10 and 37 μm at a resolution of 600 and have slit sizes of $4\overset{''}{.}7\times11\overset{''}{.}3$ and $11\overset{''}{.}1\times22\overset{''}{.}3$, respectively. The data were taken using the Staring Mode observing template that produces spectra in two *nod* positions. The separation between the *nod* positions is $3\overset{''}{.}8$ for SH and $7\overset{''}{.}4$ for LH. The observations were centered on the nucleus of the galaxies (see Figure 1) at the coordinates given in Table 1. However, as can be seen in Figure 1, the observations of NGC 520 and Mrk 52 are slightly mispointed with the SH slit measuring part of the nucleus. In NGC 3310, the mispointing is more severe and affects both modules and therefore any information we give about this galaxy in the paper refers to the position we measured and not the nucleus. Mrk 266 is also mispointed but the LH module is large enough to contain the whole galaxy and for the SH module we made use of an observation of another *Spitzer* program in which the source is well centered (PID = 3237, AORkey = 10510592). The area covered by the SH slit is equivalent to a spatial scale of about 0.085 kpc to 3.2 kpc, depending on the distance to the objects in our sample. No dedicated background observations were made. This means that there will be a small contribution of the zodiacal light to the spectra in Figures 2, 3, and 4. This has no consequence for the line measurements. Foreground emission of PAHs from our MW is also possible but this is much fainter than the targets themselves. For information of the mid-infrared continuum properties the reader is referred to the paper on the low-resolution spectra (Brandl et al. 2006) where the background contribution to the continuum has been subtracted from the spectra.

3. DATA REDUCTION AND ANALYSIS

The data were processed using version s15.3 of the *Spitzer* Science Center's pipeline which is maintained at Cornell and

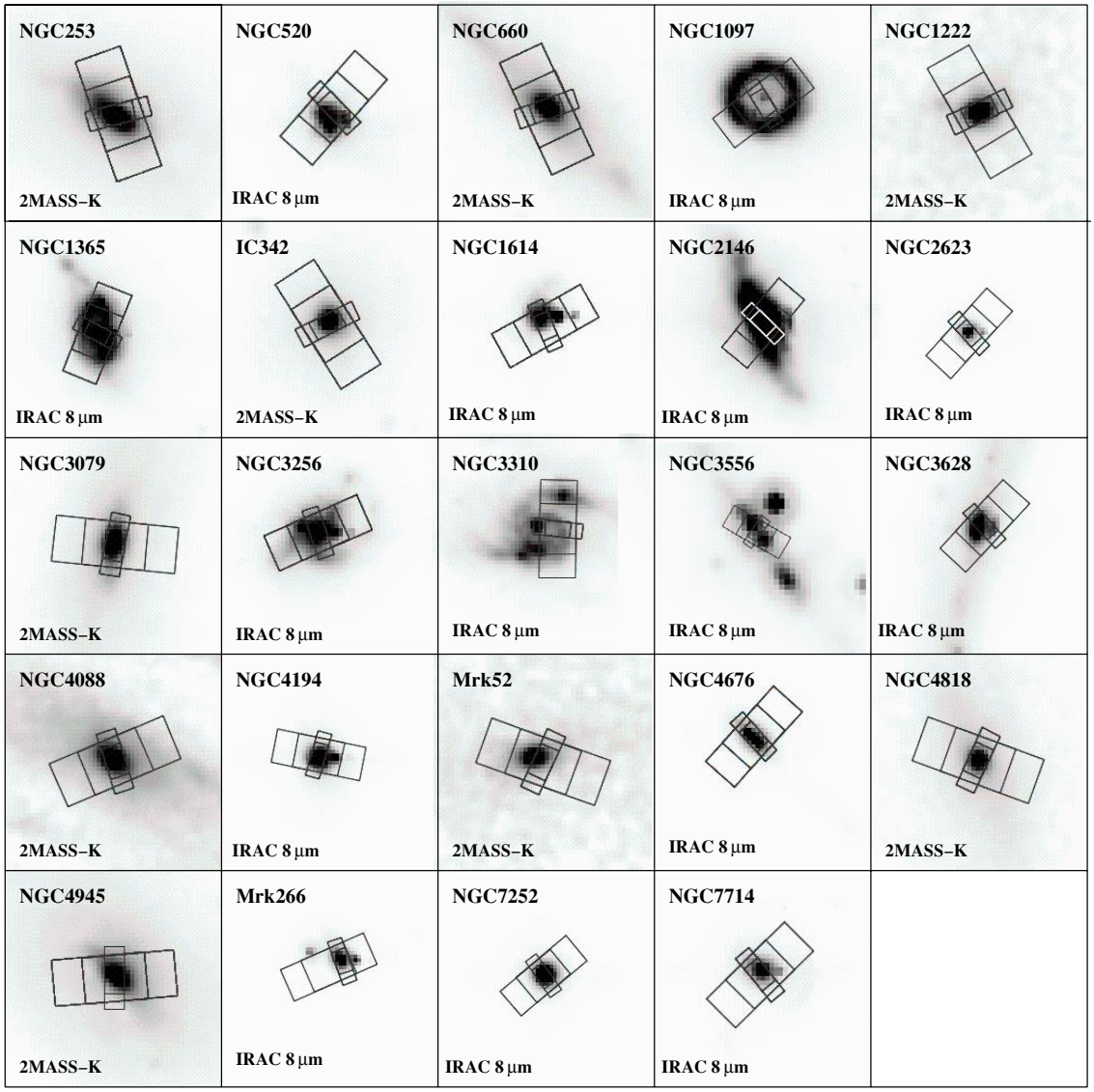

Figure 1. IRAC 8 μm and 2MASS-K images of the targets with the SH and LH slits overlaid on them. The gray scale of the image is linear up to the 50% level of brightness and is black above it.

using a script version of *Smart*[11] (Higdon et al. 2004). The reduction begins from the *droop* images which are equivalent to the more commonly used *bcd* data but without flat-field and stray-cross-light corrections. Unstable sensitive pixels (usually referred to as "rogue" pixels) were replaced using the SSC tool *irsclean*,[12] which uses campaign-based pixel masks to identify the bad pixels. At the location of a pixel identified as bad, the empirical profile in the cross dispersion direction is determined using the average profile in the neighboring rows. This profile is then scaled to the profile of the row containing the bad pixel using the remaining good pixels of that row. The rogue pixels are then replaced by the value given by the empirical profile. This method of replacing bad pixels is equivalent to interpolation when the bad pixel is located on the wings of the spatial profile but it has a definite advantage over interpolation when the bad pixel is located at the maximum of the spatial profile.

For each module the individual observations were averaged together, and spectra extracted using full aperture extraction. Flux calibration was performed by dividing the averaged spectra by the spectrum of the calibration star ξ Dra (extracted in the same way as the target) and multiplying by its theoretical template (Cohen et al. 2003, G. C. Sloan et al. 2010, in preparation). Fringes, when present, were removed using the IRS de-fringing tool *irsfringe*.[13] Finally, the spectra for each *nod* position were combined. It is worth mentioning that in six of the starbursts (IC 342, NGC 520, NGC 1097, NGC 1614, NGC 3310, and NGC 3628) the continua differed between *nod* positions. These sources are extended (see Figure 1), and this difference may reflect the different regions the *nod* positions are sampling. Since we are interested in the overall properties of the emission lines and PAH bands, and differences in these quantities lie within the errors in each nod position, we combined the nod positions in these starbursts as it was done for the rest of the sample.

[11] Smart can be downloaded from http://ssc.spitzer.caltech.edu/archanaly/contributed/smart/index.html.
[12] This tool is available from the SSC Web site: http://ssc.spitzer.caltech.edu.
[13] This contributed software can be downloaded from http://ssc.spitzer.caltech.edu/archanaly/contributed/irsfringe/.

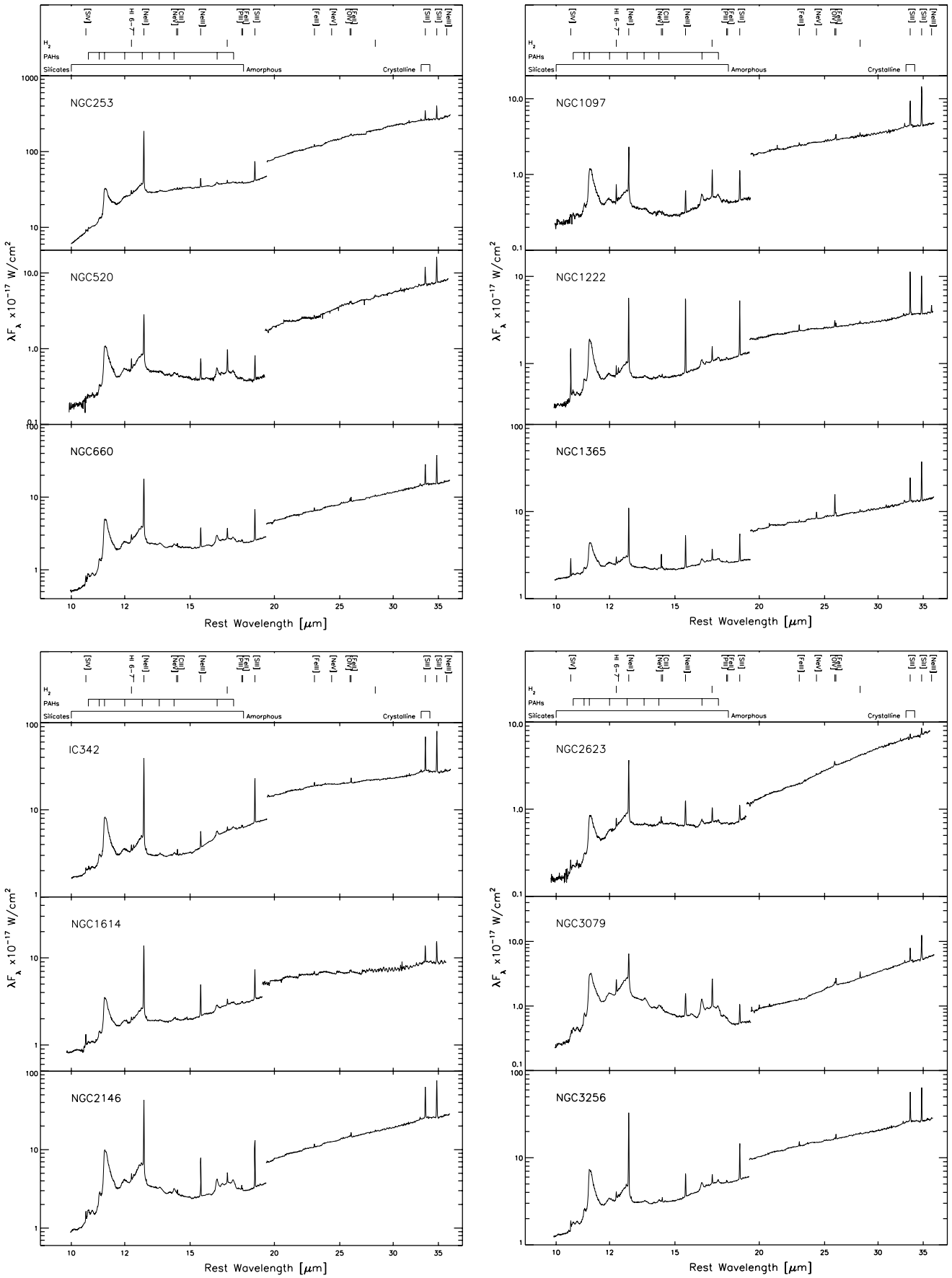

Figure 2. SH and LH spectra. The main lines and features are indicated in the top panel. The discontinuity around 19.5 μm is caused by the extended nature of the sources combined with the different sizes of the SH and LH apertures (see also Brandl et al. (2006), and their Figure 1).

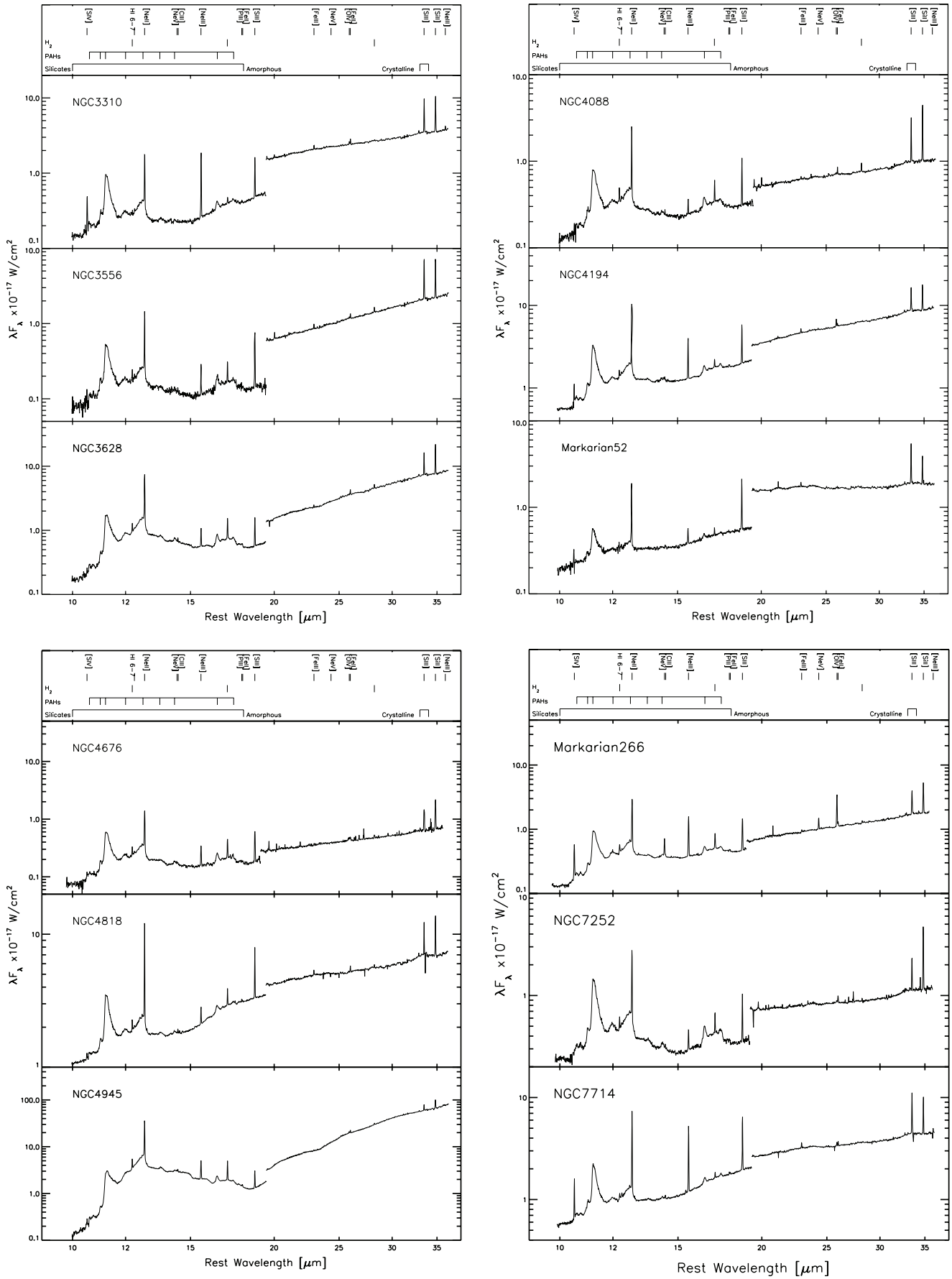

Figure 2. (Continued)

Fine-structure line fluxes are derived by fitting a Gaussian profile and integrating the flux above a local continuum. A polynomial of order 1 was used to fit the local continuum for a given line, except for the [Ne II] line which sits at the sharp flank of a PAH feature (see Figure 3). For this line, a third-order polynomial was used to fit the PAH underneath the line. This is done for each *nod* separately and then the flux in both measurements is averaged. Errors bars were estimated using the difference between the two *nod* positions or the standard deviation of the residuals of the fit, whichever is the larger. Upper-limits are derived by measuring the flux of a Gaussian with a height three times the local rms, and with an FWHM equal to the instrumental resolution. Note that, except for the line measurements of the template, Tables 2 and 3 quote the line fluxes without any normalization applied to correct for the difference in aperture between the SH and LH modules.

Following Hony et al. (2001), Vermeij & van der Hulst (2002), and Peeters et al. (2002), we have measured the strength of the PAH emission features by integrating the flux of the PAH bands above an adopted spline interpolated local continuum. For a given band the anchor points used to define the continuum (see Table 5) are the same for all sources, as are the integration limits. Spectral lines superimposed on the PAH bands were removed before integration. Our spline method for measuring PAH fluxes differs from that of *PAHFIT* (Smith et al. 2007) and others (e.g., Boulanger et al. 1998; Li & Draine 2001) by adopting a continuum (which ignores the plateau) and integrating under the bands, rather than assuming a PAH band profile and performing a simultaneous fit to all the bands. Galliano et al. (2008) concluded that both methods reveal similar trends in the data. The uncertainties in the PAH fluxes (Table 5) are based on the differences in the fluxes measured from the two individual *nod* spectra. However, this does not take into account all the systematic uncertainties (especially flux calibration). We estimate these to be 5% and choose it as our minimum uncertainty.

4. RESULTS

4.1. Individual Spectra

The spectra are shown in Figure 2. The files used to generate this plot are available in the electronic edition (in a supplementary tar.gz package). Table 4 shows an example of the format and content of tables. Measurements of fine-structure lines and PAH features that fall within the wavelength range of the IRS SH and LH modules are given in Tables 2, 3, and 5, respectively.

The spectra contain a variety of emission features. All of the spectra contain the prominent fine-structure lines of [Ne II] (12.81 μm), [Ne III] (15.55 μm), and [S III] (18.71 and 33.48 μm). Higher ionization lines such as [O IV] (25.98 μm) and [S IV] (10.51 μm) are seen in most of the sample, but are weak. The [Ne V] line at 14.32 μm is detected in seven sources. The [Ar V] line at 13.1 μm is only detected in Mrk 266. In addition, many objects show the emission of [Fe II] (25.99 μm) and [Fe III] (22.92 μm). The fine-structure lines in the IRS spectra are unresolved (even those with AGN), except for Mrk 266 and NGC 3079 where there is evidence of broadening in the [Ne II] and [Ne III] lines (H. W. W. Spoon et al. 2009, in preparation). The recombination line H I (6-7) at 12.37 μm is detected in 14 objects. Rotational lines of H_2, with the strongest transition 0-0 S(1) emitting at 17.03 μm, are present in most of the spectra. A number of PAH features are seen, the most prominent being the neutral C–H out-of-plane bending bands at 11.2 μm and the 12.7 μm. The 16.4 μm feature and 17 μm complex are also detected throughout the sample. The high-S/N allows us to detect in the spectra other weaker PAH features and a few "unidentified" bands. These are best seen in Figures 3 and 4, and are discussed in the next section.

4.2. Starburst Template

We have constructed a high-resolution starburst template spectrum from the 15 spectra in our sample with no signs of AGN activity (see Table 1). The template is available in electronic format (see Table 4). This is equivalent to the starburst template derived by Brandl et al. (2006) but using the IRS high-resolution modules. To create this template, the SH spectrum of each object was first scaled up to the LH spectrum using the overlapping continuum around 19 μm. Based on a spline-defined continuum (with anchor points given in caption of Figure 4) each spectrum were separated into a continuum-subtracted spectrum (feature spectrum) and the associated continuum spectrum (featureless spectrum). The continuum template was generated by averaging every individual continuum spectrum after normalization to the 14 μm flux. Likewise, the feature template spectrum was created by computing the noise-weighted mean of every individual continuum-subtracted spectrum, after normalization to the total flux of the emission features. Finally, the starburst template spectrum was assembled by scaling the continuum spectrum to the average ratio between the sum of the PAHs and line fluxes over the 14 μm continuum before adding it to the feature template spectrum. The template is shown in Figure 3. Up until now, the 2–40 μm *ISO*-SWS spectrum of M82 has been usually adopted in the literature as a starburst high-resolution template. However, M82 is a dwarf starburst with a low-luminosity ($3\times10^{10} L_{\odot}$) while our template is built from a sample of 15 galaxies spanning a range in IR color and luminosity typical of starburst galaxies. In fact, seven of them are LIRGS ($\geqslant 10^{11} L_{\odot}$), which in terms of galaxy evolution are much more important as they play a major role in the total energy production of the universe at $z \sim 1$ (Le Floc'h et al. 2005). The template we created may hence be more representative of the average physical parameters of local starburst galaxies, and the average line ratios and relative PAH strengths may serve as comparison data for studies of starburst galaxies at higher redshifts.

Figure 4 shows a zoom into several interesting parts of the template spectrum. Panel (a) shows that, in addition to the [S IV] line at 10.51 μm, the spectrum contains the rarely detected 10.60 μm PAH feature and an another broad feature at 10.74 μm. Panel (b) shows details of the 11.3 μm PAH feature including the 11.0 μm component. Sloan et al. (1999) noted that this feature (11.0 μm) indicates ionized PAHs based on spatially resolved spectra of the reflection nebula NGC 1333 SVS 3. Another PAH feature at 12.0 μm is seen followed by the H_2 0-0S(2) line and the H I Huα recombination line at 12.37 μm. The [Ne II] line (12.81 μm) sits in the flank of the 12.7 μm PAH feature. In panel (c), there is a PAH feature at 13.53 μm followed by an unidentified absorption feature (13.65–14.0 μm) which has, to our knowledge, not been previously detected. This absorption is detected in most of the starbursts but the strongest absorptions are found in those sources also harboring an AGN. This is shown in Figure 5, where the objects have been ordered according to the strength of the absorption feature, and where out of the bottom seven objects (those with stronger absorption), six have an AGN. Its detection in NGC 4945 is also confirmed from a map study in the region where the dip is seen to change in

Table 2
SH Line Fluxes[a]

Object	[S IV] 10.51[b]	H_2(S2) 12.28	H I(7-6) 12.37	[Ne II] 12.81	[Ne V] 14.32	[Cl II] 14.38	[Ne III] 15.55	H_2(S1) 17.03	[P III] 17.89	[Fe II] 17.95	[S III] 18.71
NGC 253	<10.50	64.32	<27.45	2832.33	<20.50	25.57	204.64	67.24	22.89	25.24	666.37
	...	6.78	...	64.20	...	5.92	9.59	2.35	6.01	5.97	14.93
NGC 520	<0.47	3.49	<0.65	44.62	<0.64	0.89	7.53	10.82	<0.51	<0.48	9.10
	...	0.22	...	1.25	...	0.15	0.21	0.35	...	...	0.59
NGC 660	2.79	12.53	<3.68	353.01	<2.26	4.05	36.96	23.52	4.89	2.52	90.02
	0.47	1.01	...	7.55	...	0.72	0.49	0.90	1.00	0.36	1.71
NGC 1097	<0.63	6.38	0.57	37.24	<0.43	<0.47	6.33	13.22	<0.99	<0.51	15.88
	...	0.50	0.11	9.27	...	...	0.18	0.36	...	...	0.40
NGC 1222	22.24	2.93	2.12	80.57	<0.57	<0.88	89.41	9.53	1.49	0.83	64.80
	0.45	0.16	0.20	1.30	...	...	1.74	0.31	0.21	0.26	1.13
NGC 1365	23.37	9.00	3.18	139.50	18.83	2.05	59.53	18.42	2.22	1.72	53.72
	1.42	0.91	0.39	3.27	0.51	0.37	0.92	0.63	0.38	0.38	3.58
IC 342	4.76	10.32	6.22	615.46	<2.41	7.99	37.20	11.69	8.27	6.55	320.03
	0.66	0.96	0.79	10.52	...	0.77	0.90	0.76	0.79	0.84	5.96
NGC 1614	6.89	5.14	1.77	249.00	<0.99	1.15	63.32	9.42	5.14	2.13	83.03
	0.54	0.51	0.37	7.00	...	0.32	1.59	0.58	0.58	0.51	2.64
NGC 2146	6.30	12.79	6.81	625.00	<2.81	5.48	91.16	26.12	7.71	3.24	190.12
	0.44	1.35	1.53	15.35	...	0.66	0.95	1.64	0.42	0.63	4.15
NGC 2623	1.20	3.15	<0.49	55.55	2.71	0.69	15.08	7.27	<0.52	<0.52	8.20
	0.15	0.19	...	0.66	0.15	0.13	0.24	0.23	...	...	0.36
NGC 3079	<0.96	23.81	<2.09	98.96	1.31	1.57	23.17	40.63	<0.52	0.90	11.83
	...	1.28	...	2.03	0.21	0.21	0.46	1.04	...	0.13	0.16
NGC 3256	5.25	15.04	6.19	514.19	<2.35	5.99	64.42	27.99	6.29	3.69	171.83
	0.57	1.07	1.38	9.34	...	0.85	0.86	2.84	0.73	0.53	2.07
NGC 3310	4.46	<0.56	0.58	27.57	<0.25	0.29	28.35	1.88	<0.61	<0.59	20.50
	0.41	...	0.13	0.61	...	0.10	0.45	0.11	...	...	0.31
NGC 3556	<0.56	1.06	0.71	21.47	<0.37	<0.40	3.23	2.90	<0.45	<0.34	12.36
	...	0.16	0.18	0.42	...	...	0.09	0.12	...	...	0.22
NGC 3628	<0.90	6.53	<1.68	125.63	0.90	2.35	10.05	16.24	<0.79	<0.96	21.32
	...	0.43	...	2.37	0.35	0.18	0.29	0.60	...	...	0.77
NGC 4088	<0.67	2.70	0.95	37.03	<0.39	0.51	2.45	4.72	<0.40	<0.37	12.50
	...	0.32	0.11	1.16	...	0.16	0.14	0.16	...	...	0.26
NGC 4194	11.46	5.03	2.12	165.47	2.96	2.49	53.99	9.25	1.70	1.90	70.92
	0.75	0.51	0.58	3.90	0.65	0.38	0.78	0.66	0.32	0.38	1.44
Mrk 52	1.02	1.50	<0.61	29.38	<0.57	<0.43	3.82	1.80	<0.45	<0.39	28.45
	0.10	0.22	...	0.53	...	...	0.29	0.19	...	...	1.63
NGC 4676	0.56	2.03	0.48	27.78	<0.25	<0.31	4.68	5.19	<0.36	<0.36	11.32
	0.06	0.14	0.09	0.96	...	...	0.16	0.32	...	...	0.37
NGC 4818	2.21	5.87	1.71	184.93	<1.21	2.27	13.73	16.83	2.61	1.41	71.96
	0.16	0.35	0.50	5.60	...	0.35	0.45	0.57	0.35	0.18	1.05
NGC 4945	0.72	33.93	<3.66	583.84	3.84	6.51	68.98	54.15	1.77	2.85	30.53
	0.18	0.85	...	12.50	0.34	0.27	14.25	4.22	0.25	0.24	0.58
Mrk 266	9.00	3.72	0.69	57.04	7.96	0.46	27.95	8.40	0.67	0.48	24.33
	0.38	0.32	0.06	1.64	0.17	0.07	0.76	0.97	0.15	0.14	0.69
NGC 7252	<0.56	2.70	<0.57	41.68	<0.33	0.56	3.72	5.10	<0.54	<0.57	11.96
	...	0.29	...	1.94	...	0.10	0.14	0.18	...	...	0.31
NGC 7714	14.76	2.85	2.18	102.55	<1.00	<0.68	77.42	4.43	2.01	1.58	81.50
	0.63	0.41	0.36	1.98	...	...	0.92	0.35	0.25	0.27	1.10
Template[c]	14.16	13.86	5.56	452.83	...	4.58	100.00	30.83	5.74	3.30	187.97

Notes.
[a] Per object, the line fluxes are given in the first row in units of 10^{-21} W cm^{-2}, with the uncertainties shown in the row below. Note that, except for the values of the template, the fluxes listed here are not to be directly compared (unless scaled) to those in Table 3 because of the different aperture used.
[b] Rest wavelength in μm.
[c] The line fluxes for the template spectrum are relative to F([Ne III]) = 100.

strength at different positions in the central region of the galaxy (H. W. W. Spoon et al. 2009, in preparation). While not reported, this dip is also present in the low-resolution starburst template (made from the same sample) in Brandl et al. (2006). The weak 14.22 μm PAH feature is present and the line at 14.36 μm corresponds to [Cl II]. Panel (d) displays more PAH features at 16.4 μm, 16.7 μm, and 17.0 μm. The H_2 0-0 S(1) transition at 17.0 μm is strong and the [Fe II] line at 17.98 μm, while weak, is still detected. Another iron line ([Fe III] at 22.93 μm) is shown in panel (e). The last panel shows a blend of lines which correspond to [O IV] (25.89 μm) and [Fe II] (25.98 μm), the stronger of which is the iron line.

Table 3
LH Line Fluxes[a]

Object	[Fe III] 22.93[b]	[Ne V] 24.31	[O IV] 25.89	[Fe II] 25.98	H_2(S0) 28.22	[S III] 33.48	[Si II] 34.81	[Ne III] 36.01
NGC 253	120.84	<73.36	154.74	250.56	<77.55	1538.03	2412.03	−243.86
	18.17	...	26.95	24.43	...	30.06	48.02	...
NGC 520	5.95	<1.42	8.10	7.56	8.23	89.44	190.71	<6.90
	0.67	...	0.88	0.78	0.60	8.60	3.41	...
NGC 660	12.33	<6.59	18.80	22.92	10.58	246.07	441.96	<8.96
	1.64	...	2.57	1.82	2.67	3.21	3.56	...
NGC 1097	4.20	<1.07	4.41	11.48	6.59	100.05	225.19	<5.29
	0.18	...	1.21	1.07	0.69	3.95	7.00	...
NGC 1222	7.04	<0.78	9.92	4.74	3.25	132.52	112.05	12.72
	0.38	...	0.48	0.38	0.34	2.30	1.70	1.30
NGC 1365	9.24	35.96	141.57	22.20	15.91	246.89	500.30	<14.78
	1.20	1.18	2.06	2.33	1.51	12.17	17.78	...
IC 342	36.43	<4.95	<7.70	51.87	<9.10	672.46	985.73	<29.96
	2.69	...	...	1.89	...	7.28	10.29	...
NGC 1614	13.14	<3.27	8.68	12.99	<8.98	101.06	148.60	12.15
	2.10	...	0.85	1.15	...	2.11	4.11	3.44
NGC 2146	23.05	<3.70	19.33	52.69	16.66	848.02	1209.35	<60.59
	2.58	...	4.48	4.59	2.33	36.93	21.70	...
NGC 2623	<1.31	2.21	9.62	2.23	<2.08	13.78	28.74	<9.41
	...	0.14	0.72	0.51	...	1.41	1.89	...
NGC 3079	1.54	<0.91	8.45	14.57	11.02	56.88	173.51	<7.05
	0.21	...	0.84	0.62	0.75	2.70	5.83	...
NGC 3256	31.55	<3.85	12.23	33.56	12.70	484.64	623.37	<33.15
	2.77	...	3.02	1.82	1.32	13.79	9.81	...
NGC 3310	5.66	<1.00	4.03	8.78	<2.32	106.02	143.54	8.01
	0.59	...	0.64	0.74	...	1.17	1.58	1.19
NGC 3556	2.24	<1.18	<1.50	3.14	4.55	96.37	96.44	<3.00
	0.34	...	...	0.47	0.47	1.18	0.80	...
NGC 3628	3.69	<1.03	<2.37	11.96	11.57	149.93	277.55	<10.09
	0.60	...	...	1.07	0.42	2.20	7.75	...
NGC 4088	0.98	<0.50	0.73	2.15	3.38	35.02	63.33	<1.33
	0.09	...	0.21	0.27	0.23	0.41	0.73	...
NGC 4194	9.96	4.04	27.45	8.48	<2.66	151.01	185.82	<10.83
	1.00	0.23	1.63	0.96	...	1.65	3.31	...
Mrk 52	4.53	<0.83	1.31	1.90	<1.35	60.43	38.02	<2.44
	0.61	...	0.23	0.31	...	1.07	0.60	...
NGC 4676	<0.58	<0.33	1.37	1.78	1.89	23.95	41.27	<2.49
	...	...	0.23	0.22	0.25	1.51	1.42	...
NGC 4818	7.96	<1.96	<1.59	10.83	4.68	80.54	128.66	<5.61
	0.50	...	...	0.88	0.51	2.44	1.97	...
NGC 4945	8.69	<7.95	47.85	55.21	44.56	338.91	846.23	−160.25
	2.09	...	6.95	5.35	8.72	70.93	50.98	...
Mrk 266	2.15	11.12	52.94	4.35	<1.60	50.93	87.02	...
	0.29	0.59	5.66	0.70	...	2.91	4.44	...
NGC 7252	1.36	<0.51	1.33	3.12	1.10	24.75	70.53	<2.20
	0.26	...	0.25	0.20	0.33	0.47	0.43	...
NGC 7714	7.88	<1.77	5.51	5.93	<1.84	115.90	102.97	7.45
	0.70	...	0.94	0.54	...	2.45	1.63	1.29
Template[c]	11.25	...	7.85	16.07	9.51	267.16	364.23	8.10

Notes.
[a] For each object, the line fluxes are given in the first row in units of 10^{-21} W cm^{-2}, with the uncertainties given in the row below. Note that the fluxes listed here are not to be directly compared (unless scaled) to those in Table 2 because of the different aperture used.
[b] Rest wavelength in μm.
[c] The line fluxes for the template spectrum are relative to F([Ne III]) = 100.

5. DISCUSSION

5.1. Conditions in the Ionized Gas

The presence of individual lines can set constraints on the ionization conditions in the hot gas in our sample. The most notable of these is [Ne V]. The [Ne V] has a high ionization potential (IP) of 97.1 eV and has never been detected in purely stellar environments, but is routinely detected in spectra of galaxies hosting an AGN (Sturm et al. 2002; Lutz et al. 2003; Weedman et al. 2005; Dale et al. 2006) and in about half of the 53 ULIRGs analyzed by Farrah et al. (2007) using *Spitzer* data. This line is also seen in young supernova remnants (Oliva et al. 1999) but in starbursts, where the overall shape of the mid-IR continuum is not flat, the presence of [Ne V] would

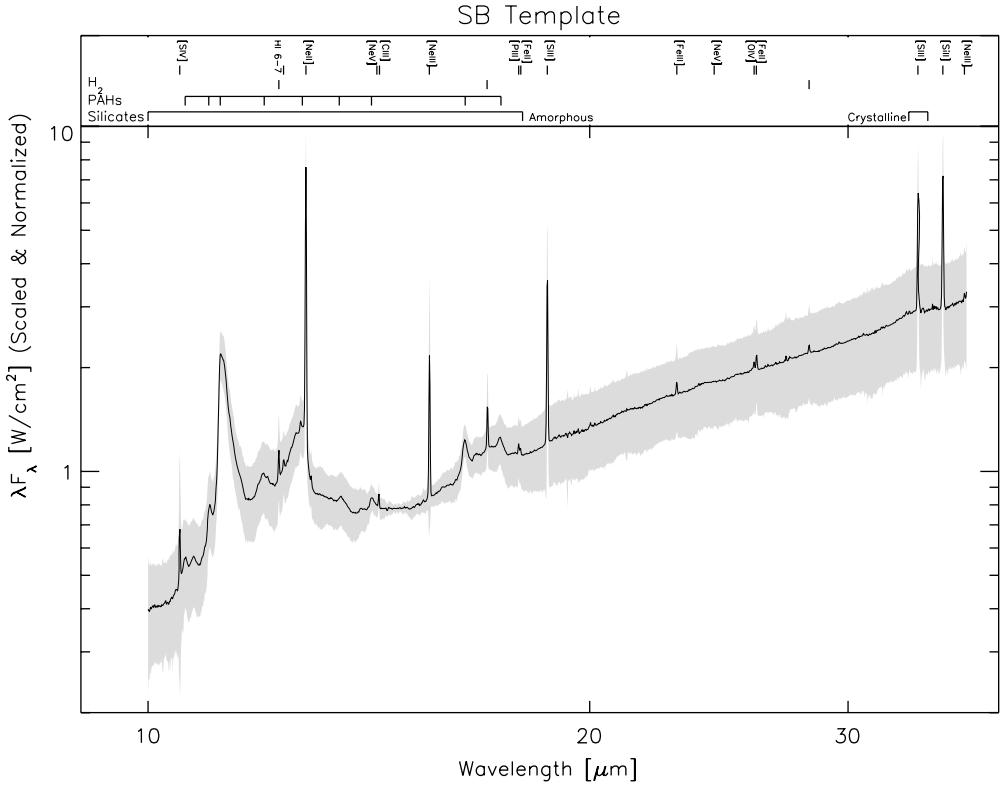

Figure 3. Template spectrum created by combining the starburst galaxies in our sample. The gray area is the standard deviation in the mean indicating the spectral diversity of the starburst sample.

Table 4
Spitzer/IRS Spectrum of NGC 253

λ (μm)	Flux (Jy)	σ (Jy)
10.0010	2.0231E+00	1.3404E-02
10.0087	2.0244E+00	2.0704E-02
10.0164	2.0571E+00	3.4718E-02
10.0241	2.0622E+00	2.5947E-02
10.0318	2.0616E+00	1.4040E-02

Notes. The full data is available in a tar.gz package in the online edition of the journal. It contains the *Spitzer*/IRS spectra for each galaxy in a separate machine-readable table (see the accompanying ReadMe file). A portion of one table is shown here for guidance regarding form and content.

(A supplementary tar file of machine-readable tables is available in the online journal.)

imply a weak AGN rather than SNe emission (the lifetime of the latter is too small to allow for a substantial contribution to the spectrum). From the objects listed in Table 2 previously known to have an AGN component in the literature, the [Ne v] line is present in Mrk 266, NGC 1365, NGC 2623, NGC 3079, NGC 3628, and NGC 4945 (see also Dudik et al. 2007), but not in NGC 660 and NGC 1097. In these two galaxies the [Ne v]14.3 μm/[Ne ii]12.8 μm line ratio is <0.07 hinting at an AGN contribution of less than a few percent using the diagram by Farrah et al. (2007, their Figure 16). NGC 1097 is a particularly interesting case; it also does not show [O iv] or [S iv], hence the AGN is likely very weak in the mid-IR. It either has a complex extinction pattern around it or it is overwhelmed by the starburst. We further detect [Ne v] in NGC 4194, which has no previous AGN classification.

The strongest detections of [Ne v] relative to [Ne ii] in our sample are found in Mrk 266 and NGC 1365, at ratios of 0.140 ± 0.005 and 0.135 ± 0.005, roughly a factor of 10 above the rest of the sample. Adopting the AGN–starburst mixing scenarios of Sturm et al. (2002) and Farrah et al. (2007), this would imply the AGN contribution to be 10 times larger in these two sources compared to the rest of the sample.

Two other individual lines are worth mentioning: the [S iv] line and the 18 μm and 26 μm [Fe ii] lines. The [S iv] line is present in most of the objects but is always weak. The line has an IP of 34.8 eV, below that of the [Ne iii] line, and therefore should be easily excited. However, the photoionization cross section of S^{3+} is lower than Ne^{2+}, and one needs many photons to produce the [S iv] line. The IP of Fe ii is even lower, at 7.87 eV. It could therefore ionize within the photo-dissociation region (PDR). Lebouteiller et al. (2008) have shown that this ion correlates well with the [Ar ii] line which is a good tracer of the ionized gas near the PDR.

Fine structure lines of the same species but from different ionization stages can be used to trace the properties (hardness and ionization parameter) of the ionizing radiation field. The diamond symbols in Figure 6 show the ratio of the [S iv]10.5 μm (IP = 34.8 eV) and [S iii]18.7 μm (IP = 23.3 eV) lines plotted against the ratio of the [Ne iii]15.5 μm (IP = 41.0 eV) and [Ne ii]12.8 μm (IP = 21.6 eV) lines for the starburst sample. As expected both ratios trace each other. Exceptions are Mrk 266 and NGC 1365. These two outliers have a strong AGN contribution to the neon lines, as measured by their >10 times elevated [Ne v]/[Ne ii] ratio compared to the other sources. Excluding these two sources, the slope for the correlation between [S iv]/[S iii] and [Ne iii]/[Ne ii] is 0.25 ± 0.03. Our values fall within the range of values found by Verma et al. (2003) in their *ISO* study of starburst galaxies (including NGC 1365). Figure 6 also includes representative subsamples of Blue Compact Dwarf Galaxies (BCDs Hao et al. 2009), ULIRGs

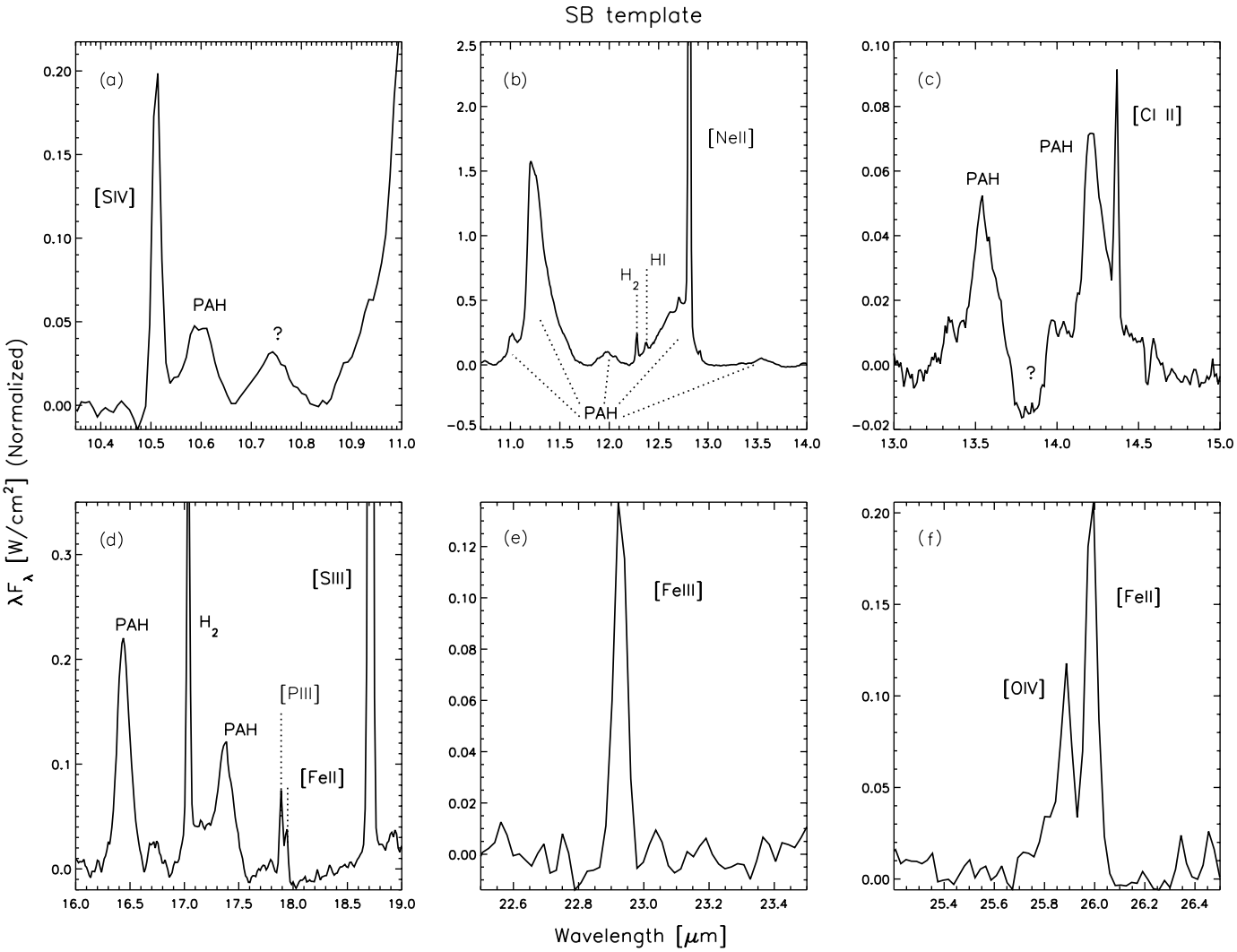

Figure 4. Closeups of the continuum-subtracted template spectrum. The anchor points used to remove the continuum in the individual spectra to create this template are those used for the PAH integration (see the caption to Table 4) plus the following points: 18.4, 19.4, 21, 22.5, 23.2, 25.0, 26.5, 28.0, 30.0, 32.0, 35.5, and 36.5 μm.

(Farrah et al. 2007), and galaxies from the *Spitzer* Infrared Nearby Galaxy Survey (SINGS Dale et al. 2009). The ratios in the SINGS galaxies studied by Dale et al. (2009) and in several star-forming regions in irregular galaxies analyzed by Hunter & Kaufman (2007) follow the trend of the starburst sample. The ratios in the starburst galaxies are lower than the BCD sample studied by Wu et al. (2008), and in fact Figure 6 shows only the lowest BCD ratios from their sample. Hao et al. (2009) compare in detail our starburst sample with similarly analyzed samples of ULIRGs, BCDs, and AGNs. They find that the starburst galaxies have the lowest excitation and are located in the lower branch of this diagram. Compared to the starburst and ULIRG samples of Verma et al. (2003) and Farrah et al. (2007) the excitation level in our sample is on the low and middle end, with the highest ratios being [S IV]/[S III] $\sim$ 0.4 and [Ne III]/[Ne II] $\sim$ 1, and the Verma et al. (2003) and Farrah et al. (2007) samples reaching values as high as 10 for both ratios. This lower ionization in our sample may indicate that there are fewer massive stars or that they are older. Interestingly, the three sources with the highest [Ne III]/[Ne II] ratios in our sample (>0.6) are not those with an AGN component, but pure starbursts. NGC 1222, NGC 3310, and NGC 7714 all are found on the "BCD branch" of the [Ne V]/[Ne II] versus [Ne III]/[Ne II] diagnostic diagram of Hao et al. (2009).

Groves et al. (2008) studied the relation between the well known mid-infrared ionization diagnostic with the ground accessible ratio of [S IV]/[Ne II]. They found a good correlation between the ratios in their sample, which included starburst galaxies, BCDs, ULIRGs, AGNs, Planetary Nebulae, and Galactic and extra-galactic H II regions. We confirm this relation (Figure 7), and find a slope value of 0.68 $\pm$ 0.08 (excluding NGC 4945), in good agreement with the slope found by Groves et al. (2008; 0.65 for the starburst subsample and 0.81 for their full sample). NGC 4945 has the strongest silicate absorption feature of the sample (Brandl et al. 2006) and this attenuates the [S IV] line flux relative to the [Ne II] line which is exactly what is seen in Figure 7.

Ho & Keto (2007) illustrated how the neon lines in the mid-infrared spectra can be a powerful indicator to derive the star formation rate in star-forming galaxies. They showed that the sum of the luminosities of both lines correlates well with the infrared luminosity in over five orders of magnitude in luminosity, and proposed a calibration between the luminosity of the lines and the star formation rate. Figure 8 shows the relation between the neon lines and infrared luminosity. Our data cover

Table 5
PAH Fluxes[a,b]

Object	F(10.6)[c]	F(10.7)[d]	F(11.0)	F(11.3)	F(12.0)	F(12.74)	F(13.5)	F(14.2)	F(16.45)	F(16.74)	F(17.0)
NGC 253	...	3.39	19.00	405.27	18.67	257.50	19.85	13.78	23.67	...	15.86
	...	0.35	1.24	20.26	2.30	12.88	2.16	3.30	4.98	...	6.98
NGC 520	0.23	0.08	0.91	17.21	1.11	9.66	0.34	0.32	0.86	0.03	1.36
	0.02	0.02	0.05	0.86	0.06	0.48	0.06	0.02	0.13	0.01	0.07
NGC 660	0.52	0.77	6.07	83.40	4.60	43.45	1.05	2.09	5.64	...	4.06
	0.21	0.10	0.30	4.17	0.44	2.17	0.26	0.22	0.32	...	0.38
NGC 1097	0.30	...	1.17	18.84	0.99	6.32	0.29	0.32	1.06	...	0.99
	0.02	...	0.06	0.94	0.05	0.32	0.07	0.02	0.23	...	0.05
NGC 1222	0.66	0.26	2.72	27.56	1.09	9.69	0.38	0.27	1.54	0.33	1.53
	0.12	0.08	0.14	1.38	0.18	0.48	0.10	0.09	0.17	0.13	0.22
NGC 1365	0.70	0.51	3.64	51.38	2.45	20.04	1.14	0.65	2.64	0.31	3.20
	0.50	0.28	0.46	2.57	0.49	1.08	0.23	0.27	0.32	0.23	0.46
IC 342	1.41	0.64	9.70	119.19	6.38	47.77	3.04	3.26	6.21	...	4.67
	0.16	0.11	0.49	5.96	0.32	2.39	0.15	0.16	0.45	...	0.23
NGC 1614	1.18	0.12	3.82	47.29	2.46	22.80	0.30	1.98	3.35	0.34	3.93
	0.06	0.03	0.19	2.36	0.12	1.14	0.11	0.10	0.60	0.03	0.20
NGC 2146	1.38	1.36	14.80	168.24	7.03	84.87	1.58	4.69	9.94	1.19	12.16
	0.21	0.13	0.74	8.41	0.41	4.24	0.31	0.36	0.50	0.36	0.75
NGC 2623	0.29	0.15	0.91	12.61	0.63	7.37	0.43	0.40	1.13	...	0.74
	0.04	0.02	0.05	0.63	0.06	0.37	0.03	0.03	0.06	...	0.07
NGC 3079	...	...	3.22	56.68	3.13	35.39	1.58	1.59	5.07	0.24	3.41
	...	...	0.16	2.83	0.16	1.77	0.08	0.08	0.25	0.02	0.17
NGC 3256	1.31	0.86	8.65	108.19	5.41	50.18	1.50	1.69	7.77	0.99	6.27
	0.31	0.17	0.43	5.41	0.30	2.51	0.12	0.13	0.43	0.29	0.55
NGC 3310	...	...	1.21	14.79	0.48	5.03	0.44	0.31	0.78	0.08	0.74
	...	...	0.06	0.74	0.02	0.25	0.02	0.02	0.10	0.01	0.04
NGC 3556	...	...	0.84	8.46	0.46	3.17	0.31	0.29	0.44	...	0.44
	...	...	0.04	0.42	0.02	0.16	0.05	0.01	0.11	...	0.03
NGC 3628	0.02	0.23	1.81	29.98	1.48	19.88	0.01	0.63	2.04	0.19	2.38
	0.02	0.01	0.09	1.50	0.07	0.99	0.14	0.03	0.27	0.01	0.12
NGC 4088	...	...	1.21	12.64	0.66	5.09	0.17	0.22	0.93	...	0.68
	...	...	0.06	0.63	0.03	0.25	0.01	0.02	0.09	...	0.03
NGC 4194	0.88	0.27	4.84	49.18	1.55	20.15	...	1.00	2.83	0.31	3.19
	0.14	0.09	0.24	2.46	0.21	1.01	...	0.16	0.19	0.15	0.27
Mrk 52	...	...	0.64	5.88	0.43	2.49	...	0.17	0.35	...	0.31
	...	...	0.07	0.29	0.08	0.12	...	0.03	0.04	...	0.05
NGC 4676	0.23	...	0.79	9.41	0.35	4.18	0.09	0.43	0.68	0.05	0.68
	0.02	...	0.04	0.47	0.03	0.21	0.02	0.02	0.03	0.02	0.06
NGC 4818	0.59	0.48	3.72	43.53	2.07	18.95	0.55	1.18	3.14	0.41	1.87
	0.11	0.03	0.19	2.18	0.12	0.95	0.09	0.06	0.16	0.10	0.17
NGC 4945	...	...	1.36	54.64	3.64	83.84	4.85	2.64	6.20	0.17	3.49
	...	...	0.13	2.73	0.57	4.19	0.24	0.13	0.31	0.06	0.17
Mrk 266	0.25	0.12	1.09	14.90	0.73	7.13	0.13	0.57	0.84	...	1.07
	0.05	0.03	0.05	0.74	0.10	0.36	0.06	0.06	0.08	...	0.14
NGC 7252	0.14	...	2.05	23.54	1.12	7.55	...	0.50	1.31	...	1.54
	0.04	...	0.10	1.18	0.06	0.38	...	0.05	0.07	...	0.08
NGC 7714	0.52	0.27	3.18	28.21	1.53	11.34	0.22	0.50	1.83	0.21	1.81
	0.14	0.05	0.16	1.41	0.15	0.57	0.07	0.09	0.11	0.09	0.16
Template[e]	1.24	0.59	8.57	100.00	4.65	41.26	0.61	1.31	6.58	0.47	5.04

Notes.
[a] PAH fluxes and uncertainties (in the row below the measurement) in units of 10^{-20} W cm^{-2}.
[b] The anchor points for the continuum were selected at these positions: 10.21, 10.38, 10.64, 10.83, 11.74, 12.21, 13.08, 13.47 μm for PAHs between 10 and 13 μm; 13.01, 13.29, 14.55, 14.70 μm for PAHs between 13 and 15 μm; and 15.64, 15.83, 16.10, 16.61, 16.90, 17.70 μm for PAHs between 16 and18 μm. The integration limits for the PAHs (in the same order as they are in the table) are 10.42–10.66, 10.66–10.83, 10.85–11.1, 11.1–11.7, 11.74–12.20, 12.20–13.1, 13.4–13.68, 13.9–14.1, 16.2–16.62, 16.62–16.88, and 16.9, 17.55 μm.
[c] PAH position in parenthesis in μm.
[d] The identification of this feature is not known, but for simplicity we fold its measurement into this table.
[e] The fluxes of PAH features in the template have been normalized so that F(11.3) = 100.

a narrow range of infrared luminosities, but it can be seen that a correlation is present. The slope in the figure has a value of 1.18 ± 0.20, agreeing within the errors with that reported by Ho & Keto (2007; 0.98 ± 0.069).

5.2. Abundances

Infrared lines offer many advantages over optical or ultraviolet (UV) lines for measuring elemental abundances, the most

Table 6
Elemental Abundances[a]

Object	S^{2+}/H (10^{-6})	S^{3+}/H (10^{-7})	Ne^{+}/H (10^{-4})	Ne^{++}/H (10^{-5})	Fe^{+}/H (10^{-6})	Fe^{++}/H (10^{-6})	ICF Fe IV	S/H^{b} (10^{-6})	Ne/H (10^{-4})	Fe/H (10^{-6})
NGC 1097	3.22	<0.22	0.84	0.68	1.18	0.56	1.09	3.54	0.91	1.90
	0.79	0.00	0.14	0.11	0.19	0.16		0.79	0.15	0.35
NGC 1222	3.53	2.09	0.49	2.58	0.40	0.78	1.58	4.09	0.75	1.87
	0.87	0.37	0.08	0.43	0.07	0.22		0.91	0.12	0.29
NGC 1365	1.96	1.47	0.56	1.15	0.56	0.31	1.17	2.30	0.68	1.02
	0.48	0.25	0.10	0.19	0.09	0.08		0.50	0.12	0.17
IC 342	5.95	0.15	1.27	0.37	1.47	1.34	1.07	6.56	1.31	3.01
	1.46	0.03	0.21	0.06	0.24	0.38		1.46	0.22	0.62
NGC 1614	5.42	0.78	1.80	2.19	2.23	2.94	1.20	6.04	2.02	6.21
	1.33	0.14	0.31	0.36	0.36	0.82		1.34	0.35	1.18
NGC 2146	3.23	0.18	1.18	0.82	0.64	0.37	1.09	3.57	1.26	1.10
	0.79	0.03	0.20	0.14	0.10	0.10		0.79	0.21	0.21
NGC 3256	3.21	0.17	1.07	0.64	0.71	0.87	1.13	3.55	1.13	1.78
	0.79	0.03	0.18	0.11	0.12	0.25		0.79	0.19	0.37
NGC 3310	4.07	1.53	0.61	2.98	1.08	0.90	1.38	4.63	0.91	2.73
	1.00	0.27	0.10	0.50	0.18	0.25		1.03	0.15	0.43
NGC 3556	2.01	<0.16	0.39	0.28	0.21	0.19	1.13	2.21	0.42	0.45
	0.50	0.00	0.07	0.05	0.04	0.06		0.50	0.07	0.09
NGC 4088	1.53	<0.14	0.50	0.16	0.30	0.18	1.06	1.68	0.52	0.51
	0.37	0.00	0.09	0.03	0.05	0.05		0.37	0.09	0.10
NGC 4194	3.86	1.08	1.00	1.56	0.69	1.06	1.25	4.35	1.16	2.19
	0.95	0.18	0.17	0.26	0.11	0.30		0.97	0.20	0.41
NGC 4676	2.74	0.23	0.75	0.60	0.65	0.00	1.00	3.04	0.81	0.65
	0.68	0.04	0.13	0.10	0.11	0.00		0.68	0.14	0.11
NGC 4818	4.87	0.26	1.39	0.49	2.09	1.99	1.08	5.38	1.44	4.43
	1.20	0.04	0.23	0.08	0.35	0.58		1.21	0.24	0.92
NGC 7714	4.32	1.35	0.60	2.17	0.71	1.22	1.43	4.89	0.82	2.76
	1.06	0.24	0.10	0.37	0.12	0.34		1.08	0.14	0.46
Solar[c]	...	...	...	...	...	...	...	14-21	0.7-1.2	32.4

Notes.
[a] Abundances are given in number with the uncertainties indicated in the row below each measurement.
[b] Includes 10% of S III to account for the contribution of S II (see Section 5.2).
[c] Range of solar abundances taken from Grevesse & Sauval (1998), Feldman & Widing (2003), Asplund et al. (2005), and Asplund et al. (2006). See Section 5.2 for explanation.

important of which is their small dependence on the electron temperature (e.g., Bernard-Salas et al. 2001; Wu et al. 2008). This reduces the uncertainty in the abundance estimates when there are electron temperature variations, which is the case in integrated spectra of galaxies, or when the electron temperature cannot be measured. IR lines are also less affected by extinction. Optical and UV studies also rely on the often rather uncertain, ionization correction factors (ICFs) to account for unobserved stages of ionization. The direct measure of important stages of ionization of some elements in the infrared greatly reduces, or completely avoids, the use of ICFs.

The H I (6-7) line at 12.37 μm is detected in 14 of the stabursts. This allows us to measure the abundances of neon, sulfur, and (tentatively) iron relative to hydrogen. The abundances are derived adopting an electron temperature (T_e) of 10,000 K and a gas density of 100 cm^{-3}. These are values typical of H II regions. We derived abundances for a range of T_e (7500–12,500 K), and used the differences to obtain the uncertainties in the measurements. These uncertainties amount to around 20% in the total abundances. Using these parameters and solving the equation of statistical equilibrium for the levels of the atoms, the ionic abundance can be derived (see Equation (1) Bernard-Salas et al. 2001). These values are reported in Table 6. Note that we cannot derive the density from the pair of [S III] (18.7 μm/33.4 μm) or [Ne III] (15.5 μm/36.0 μm) lines because the dependence of these ratios on the density starts above 3000 cm^{-3} for the sulfur ratio, and higher for the neon ratio.

Compared to our reported values, an electron density of 1000 cm^{-3} (on the high side for H II regions) will produce abundances that are no more than 1.7% higher for neon, 13% higher for sulfur, and about 80% lower for iron. The latter is due to the electronic configuration of iron.

In starburst galaxies the most important stages of ionization of neon for abundance determination are Ne^{+} and Ne^{++} which are measured in the IR. Thus, no ICFs are needed. Among the 14 objects with a H I detection, Ne^{4+} is present in NGC 1365 and NGC 4194 (Table 6), but this likely originates from the AGN given the hard radiation field needed to break the high IP barrier of 97.1 eV to produce this ion. This applies as well to the Ne^{3+} (IP of 63.5 eV, also above the double ionized helium cutoff). In addition, the contribution of Ne^{4+} to the total neon abundance is less than 1%. The [Ne V]14.3 μm/[Ne II]12.81 μm ratio in NGC 1365 and NGC 4194 is 0.13 and 0.018, respectively. These ratios correspond in the Farrah et al. (2007) and H. W. W. Spoon et al. (2009, in preparation) diagrams to an AGN contribution of $\sim$10% and <1%, respectively. This implies that the abundances we derive for NGC 4194 is indeed representative of the starburst while in NGC 1365 our abundances may be $\sim$10% too high. The total sulfur abundance is derived adding the contribution from S^{++} and S^{3+}. No S^{+} is measured in the infrared but its contribution

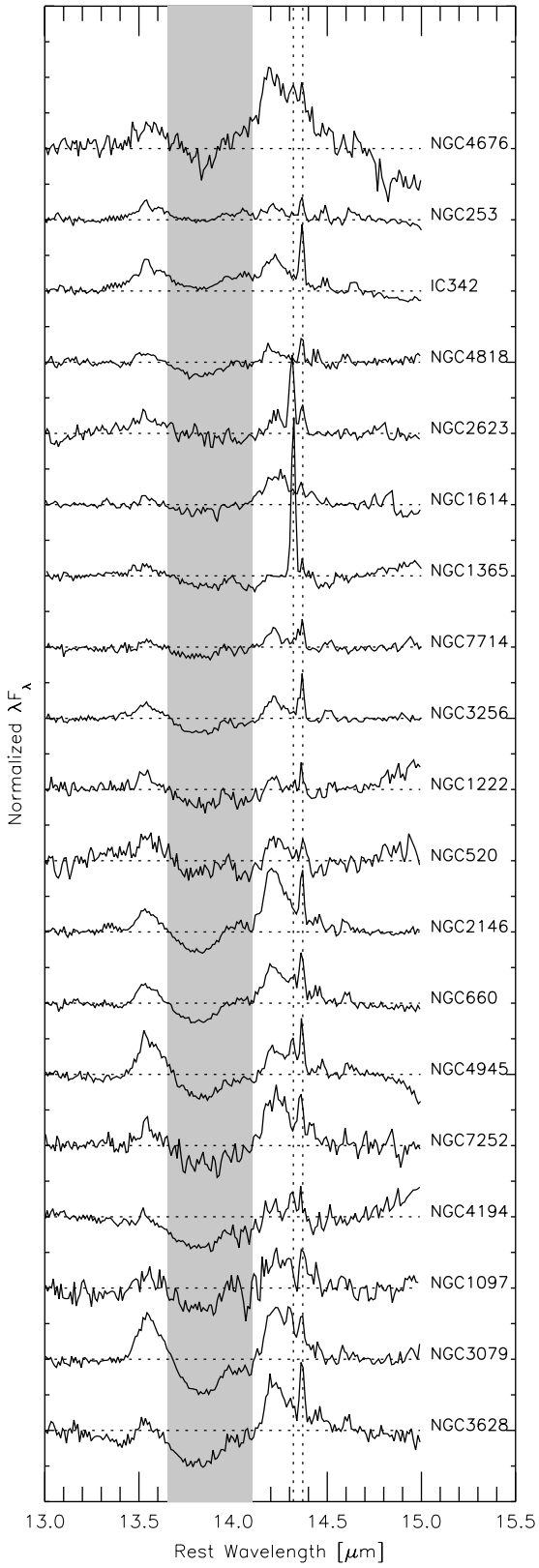

Figure 5. Continuum-divided spectrum to highlight (in gray) the absorption feature between 13.56 and 14.0 μm. The sources have been ordered by decreasing the strength of the feature. The vertical lines indicate the position of the [Ne V] and [Cl II] fine-structure lines.

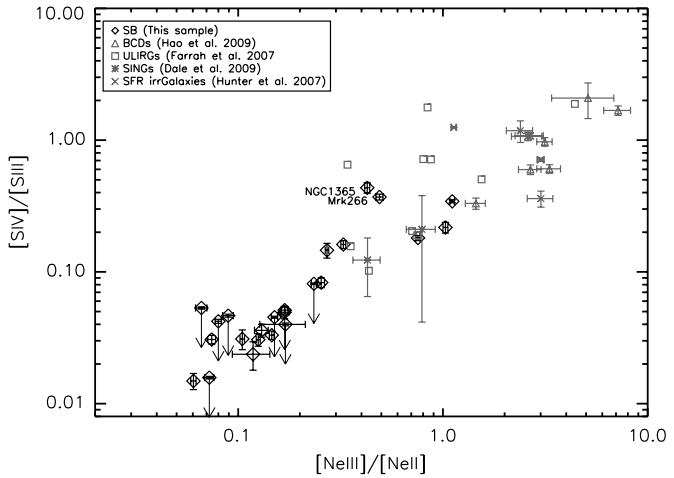

Figure 6. Hardness of the radiation field as traced by the sulfur (10.51 μm/18.71 μm) and neon (15.55 μm/12.81 μm) line ratios.

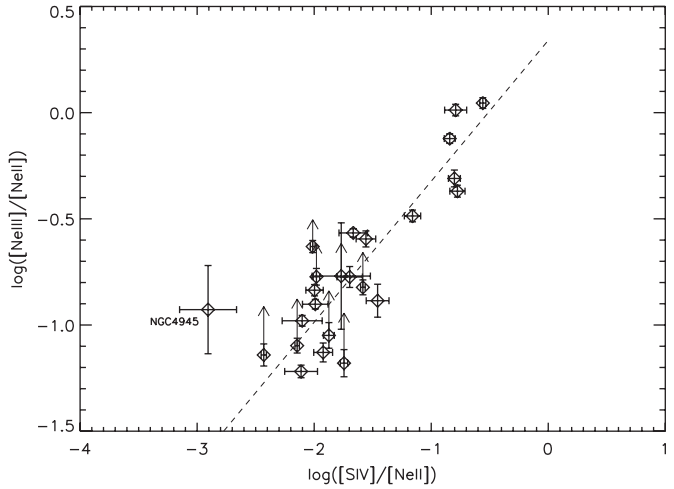

Figure 7. Hardness of the radiation field as given by the [Ne III]/[Ne II] and [S IV]/[Ne II] ratios. The dashed line indicates the best fit to the data excluding NGC 4945: $\log([\mathrm{Ne\,III}]/[\mathrm{Ne\,II}]) = -0.38(\pm0.12) + 0.68(\pm0.08) \times \log([\mathrm{S\,IV}]/[\mathrm{Ne\,II}])$.

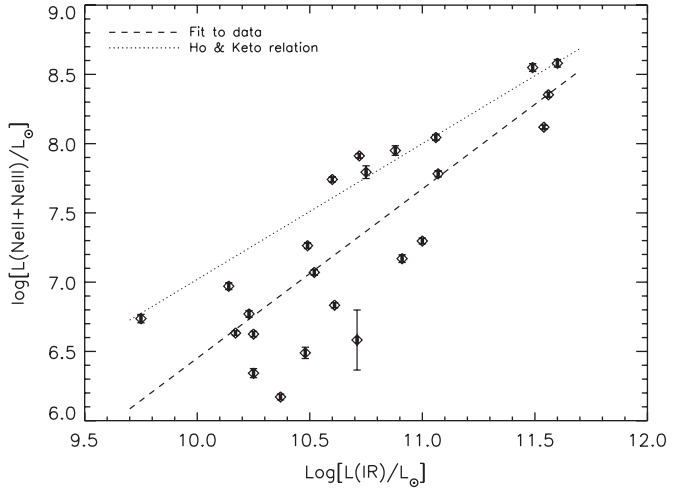

Figure 8. Sum of the [Ne II] and [Ne III] luminosities plotted against the infrared luminosity (8–1000 μm). The dashed line indicates the best fit to the data: $\log[L(\mathrm{Ne\,II} + \mathrm{Ne\,III})/L_\odot] = -5.3(\pm2.1) + 1.18(\pm0.20) \times \log[L(\mathrm{IR})/L_\odot]$.

to the total sulfur abundance is usually small. Martín-Hernández et al. (2002) estimated a contribution of about 15% of S^+ in the Galactic ultra-compact H II regions they studied. Vermeij & van der Hulst (2002) analyzed a sample of Magellanic Cloud H II regions using IR data, and combined the optical measurements of [S II] lines. They derived an ionic abundance of S^+ between

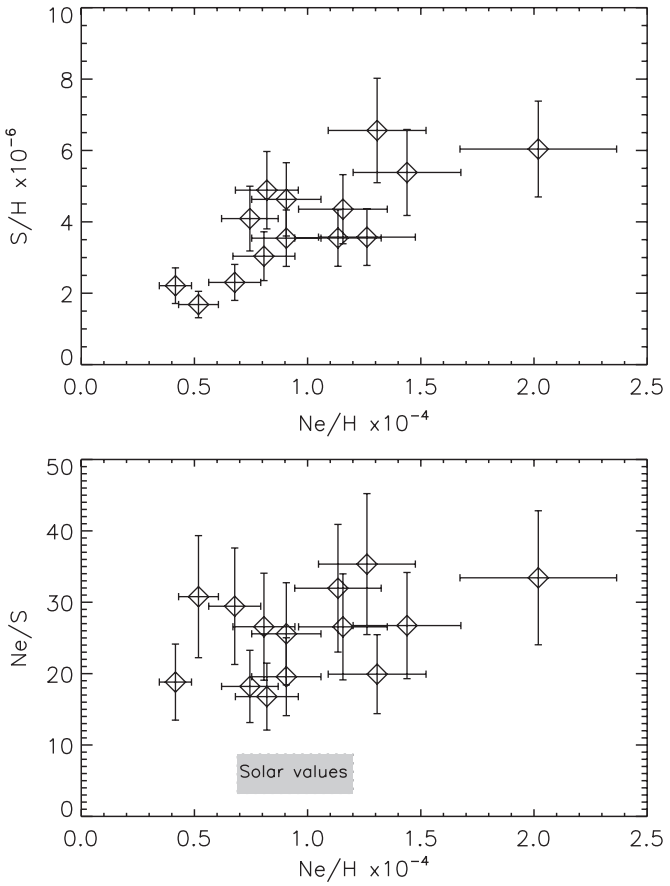

Figure 9. Abundance relations for those objects with a measured H I line in the IRS spectrum. These include 14 galaxies of which three have an AGN. Top panel: neon and sulfur abundances. Bottom panel: neon over sulfur ratio plotted against the neon abundance as an indicator of the metallicity. The gray box in the bottom panel indicates the range of solar values found in the literature (see Section 5.2). Note that the solar sulfur abundance ranges from 1.4 to 2.1×10^{-5}, which is significantly higher than the range of values in the starburst sample (top panel) and is therefore not plotted.

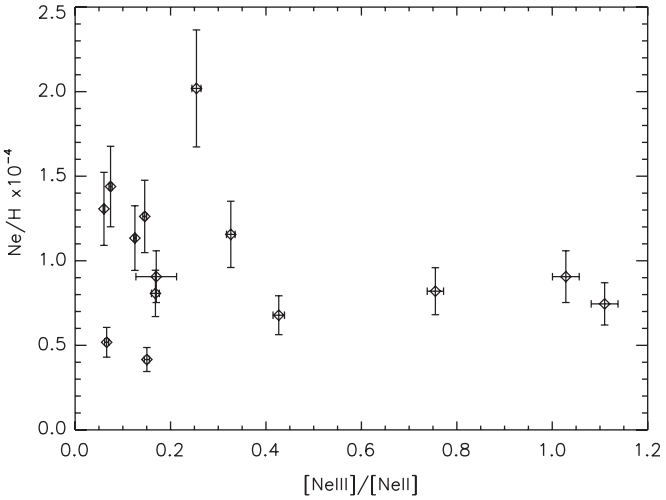

Figure 10. Neon abundance vs. the hardness of the radiation field.

2% and 20% of the total sulfur abundance, with ∼8% being the average. Using the photoionization code of Stasinska (1990) we have created a grid of models at typical conditions of H II regions; stellar temperatures considered between 37,500 and 55,000 K, and an electron density of 10 cm^{-3}, and a filling factor ranging from 0.2 to 1.0. These models predict the contribution of S^+ to be between 7% and 15% of that of S^{++} (which is the dominant contributor to the total sulfur abundance). We have thus adopted a 10% contribution of S^+ to the sulfur abundance (ICF = 1.1) to account for the contribution of this ion in our sample. While we have measured Fe^+ and Fe^{++} from our *Spitzer* data, Fe^{3+} may be an important contributor (up to half) to the total iron. Its contribution has been estimated using the photoionization grid models by Stasinska (1990), and taking advantage of the similarity in IP between the [Ne III]/[Ne II] and [Fe IV]/[Fe III] line ratios to scale the contribution of this ion in each object. At can be seen from Table 6 the ICF varies from a few percent to a factor 2. Given the importance of this ion to the total iron budget in those objects with a high ICF, the iron abundances we report should be interpreted with care. The uncertainty for this element in Table 6 only takes into account the uncertainty in the Fe^+ and Fe^{++} ionic abundance.

In Figure 9 (top), the neon abundance of our starburst sample correlates reasonably well with the sulfur abundance. This is expected because they are both α-elements and are being produced in the same type of stars. This finding was also pointed out by Wu et al. (2008) in their BCD sample and it contradicts the earlier findings of Verma et al. (2003) who based on *ISO* data did not find such a correlation between the abundance of these two elements for the starbursts they studied. In our sample the neon abundances range from slightly supersolar (IC 342, NGC 1614, NGC 4818) to several times lower than the solar value (see Table 6). Note that the solar abundances of certain elements have been subject to many changes during the last decade (Pottasch & Bernard-Salas 2006; Bernard-Salas et al. 2008; Lebouteiller et al. 2008), and thus, we resort to compare to the range of values found in the literature ($(0.69–1.2)\times10^{-4}$). There is however increasing evidence that the higher solar neon abundance reported agrees better with the findings of studies in Galactic H II regions and planetary nebulae. The sulfur abundance is also lower than solar (more so than neon, with solar sulfur values ranging from $(1.4–2.1)\times10^{-5}$), which is in agreement with many previous studies. Available optical-derived abundances of oxygen by Pilyugin et al. (2004),Pastoriza et al. (1993), and Gonzalez-Delgado et al. (1995) in IC 342, NGC 3310, and NGC 7714 (7.1, 1.5, 1.8×10^{-4}, respectively) confirm the trend of our IR-derived neon abundances, with IC 342 supersolar, and the other two galaxies having a 2–3 times lower abundance than the Sun (adopting 4.9×10^{-4} for the solar oxygen abundance).

The bottom panel in Figure 9 displays the Ne/S ratio versus the neon abundance. The range of solar values is indicated by the gray box in the figure. The Ne/S ratio varies from 18 to 40. This range of values is typical for other infrared derived abundances in starburst galaxies, H II regions, and even planetary nebulae (Rubin et al. 2007, 2008; Bernard-Salas et al. 2008). It is overall higher than the ratio found by Wu et al. (2008) in their abundance analysis of BCDs, where they find values from 10 to 20. The Ne/S ratios are higher than the solar Ne/S ratio, revealing a discrepancy between the neon and sulfur solar values, and which has now been widely reported (e.g., Marigo et al. 2003; Henry & Kwitter 2004; Rubin et al. 2007; Bernard-Salas et al. 2008; Wang & Liu 2008, and references therein). In Figure 10, the neon abundance is plotted versus the hardness of the radiation field. The sample is small but seems to indicate that a hard radiation field is found only for sources with a low metallicity which ties well with the common knowledge that at low stellar metallicity, line blanketing is diminished resulting in harder stellar radiation fields.

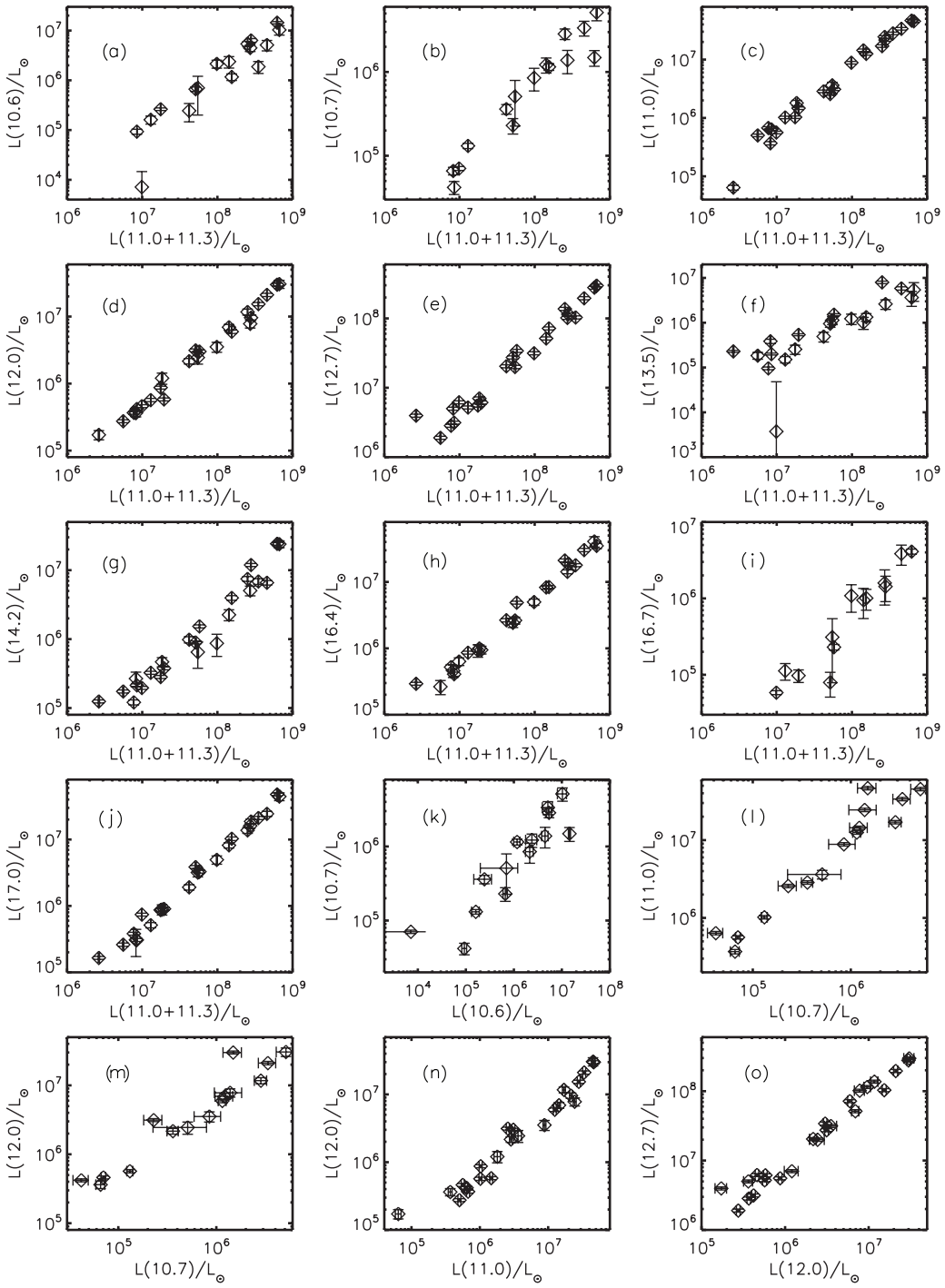

Figure 11. Correlation between the PAH bands.

5.3. PAHs

In Figure 11, the PAH luminosity for the different bands is plotted. We chose to compare the PAH features in the spectra to the integrated emission of the 11.0 + 11.3 μm complex because it is the strongest in this wavelength region (panels (a)–(j)).

Panels (e), (h), and (j) show a very good correlation of the 11.3 μm complex with the relatively strong PAH bands at 12.7, 16.4, and the 17.0 μm PAH complex. The 17.0 μm complex was discovered by Van Kerckhoven et al. (2000) as a weak feature in *ISO* spectra and attributed to PAHs by laboratory analysis (Leger & Puget 1984; Allamandola et al. 1985). Smith et al. (2007) corroborate this using spectra from the SINGS galaxies and showing good correlation between the strength of the 17.0 μm and the 11.3 μm PAH complexes. Our sample supports this finding (panel (j)). Other bands also correlate well (e.g., 11.0, 12.0, 16.7 μm). The correlation of the weaker bands (10.6, 13.5, 14.2 μm) is good but shows more scatter. The 16.7 μm feature is listed by Smith et al. (2007) as part of the 17.0 μm complex but in our higher resolution spectra we can separate it from this complex. Smith et al. (2007) also report a PAH feature at 15.9 μm. This feature is not present in our high-S/N template spectrum but may be present in NGC 3079, NGC 3628, and

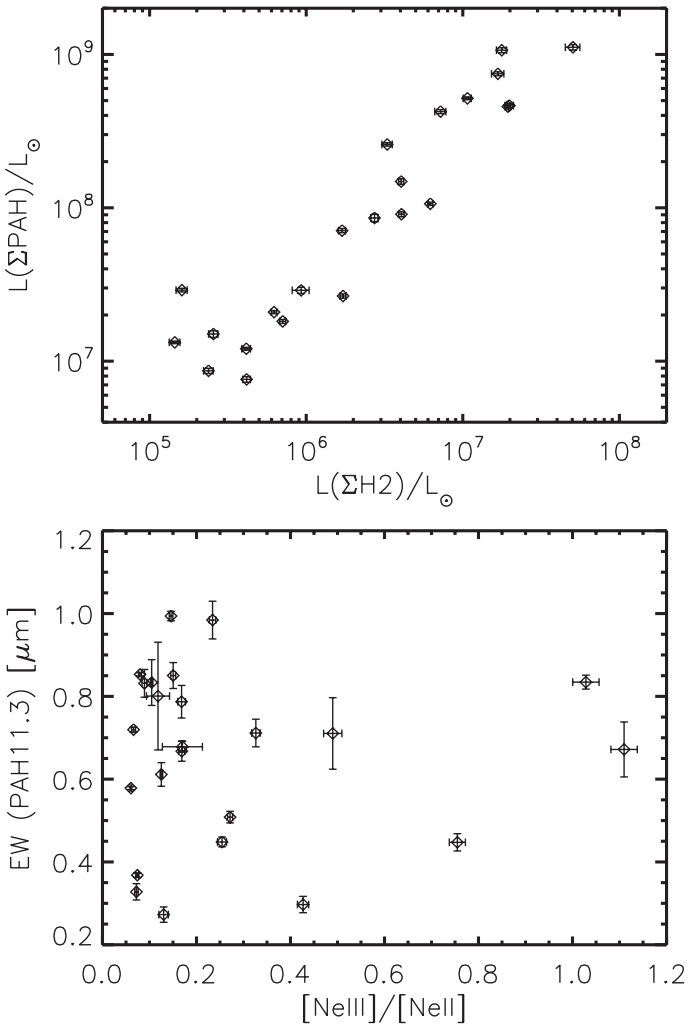

Figure 12. Top panel: sum of PAH luminosities vs. the H_2 emission. Bottom panel: the 11.3 μm PAH EW with respect to the hardness of the radiation field as given by the [Ne III]15.5 μm/[Ne II]12.8 μm ratio.

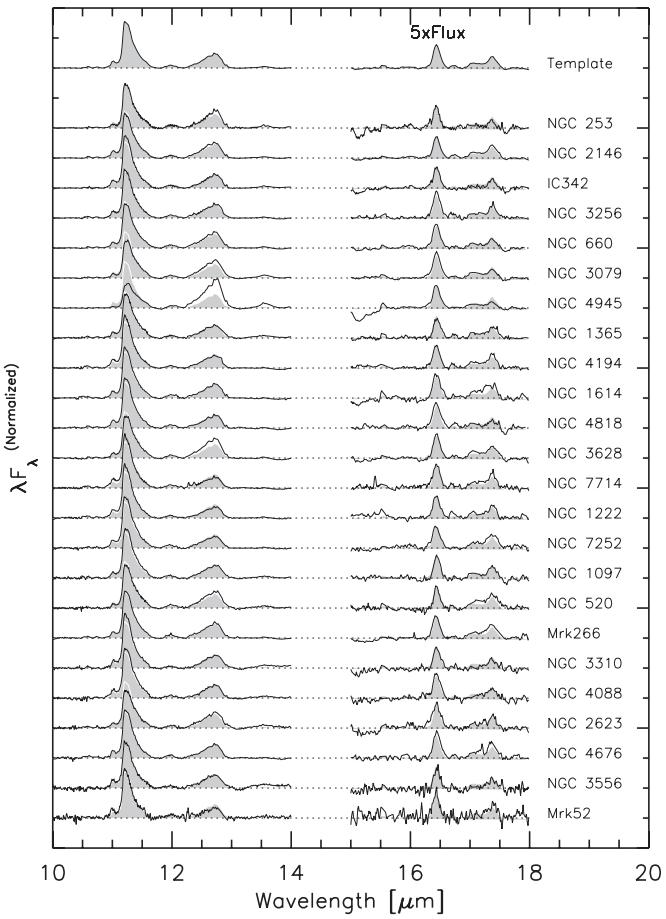

Figure 13. Continuum-subtracted spectra of the starburst sample. The thin black line represents the spectrum of the corresponding object and the gray shaded area of the template (with a white edge to distinguish the gray areas in the overlapping 11.3 μm band). The fine-structure line emission has been removed to better show the PAH profile in the starburst spectra. The spectra have been normalized to the total PAH emission and ordered according to their 11.3 μm PAH strength (strongest at top), and the 15–18 μm flux density has been multiplied by a factor of 5 to better display the PAHs in that region.

NGC 4676, albeit weakly. The unidentified feature at 10.75 μm (panel (b)) shows a good correlation with the 11.3 μm complex. In the bottom panels ((l) and (m)) we plot this feature with respect to other weak PAHs. Although there is some scatter, they do seem to correlate. It is therefore likely that the 10.75 μm feature is either a PAH or at least its carrier is carbonaceous in nature. Panel (n) shows a very good correlation between the satellite features in the 11.0 and 12.0 μm bands, and the last panel displays the equally good correlation between the 12 μm PAHs. In summary, the strengths of the PAH features scale with each other.

Figure 12 displays the relation between the PAH features and the emission lines. In the top panel, the sum of the PAH luminosities is plotted against the sum of the H_2 lines. Both are produced in the PDR, albeit in different regions, and their fluxes correlate well. In the bottom panel, the equivalent width (EW) of the 11.3 μm PAH[14] is plotted against the [Ne III] over [Ne II] line ratio. There is no correlation, indicating that there is no dependence of the PAH with the hardness of the radiation field. In fact, the EW of the 11.3 μm shows little variation in Figure 12. In AGNs, the PAH EW is seen to decrease with harder radiation field as the PAHs are further ionized or destroyed, but the PAH EW is flat for soft radiation fields as those in starbursts (V. Lebouteiller et al. 2010, in preparation).

Another characteristic of the PAHs is their profile, which has been found to change between and within sources. This led Peeters et al. (2002) to establish a classification based on the peak position of the different bands. Figure 13 shows the continuum-subtracted spectra for all the objects in the sample in the regions of interest (where the emission lines have been removed). The gray area in the figure represents the template spectrum. As opposed to the template shown in Figures 3 and 4, this template has been normalized to the sum of the PAHs (and not the sum of the PAHs plus lines), but both are very similar. This PAH continuum-subtracted spectrum of the template starburst is also available in electronic format (see Table 4). The fact that the spectrum of each object (thin black line in the figure) follows that of the template (gray area) indicates there is hardly any variation in the profiles.

The relative strength of the features is also the same for most of the objects although there are a few variations. The most striking is 12.7 μm PAH in NGC 4945 which is stronger than the 11.3 μm PAH. The reason for this is the stronger silicate dust

[14] For simplicity we use the EW of the combined 11.0 and 11.3 μm components. This is valid as both bands correlate well with each other (Figure 11).

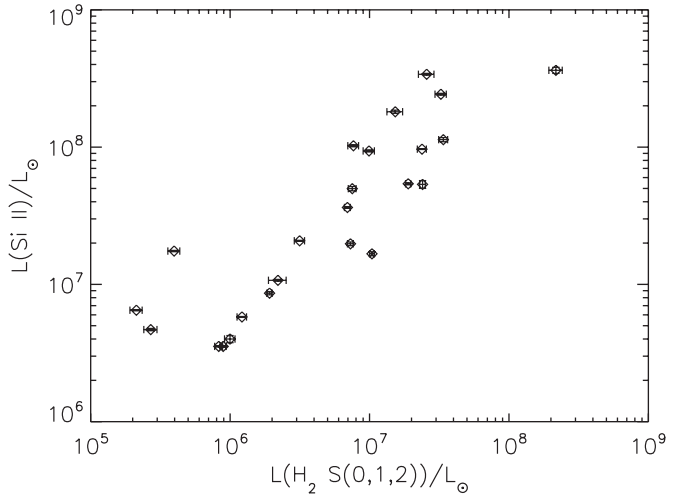

Figure 14. Luminosities of the [Si II] line vs. the sum of the three H_2 rotational lines measured in the IRS spectrum. For this plot, the fluxes of the H_2 S(2) and S(1) lines have been scaled based on the SH–LH continuum (see the text for further details).

extinction on the 11.3 μm PAH than the 12.7 μm PAH. This band is also strong (relative to the 11.3 μm PAH) in those starbursts with AGN signature (e.g., NGC 660, NGC 3079, NGC 3628) but also in a few objects with no AGN (e.g., NGC 253). The 17.0 μm complex does not always follow that trend. Despite these differences the profiles are near akin. As we saw from previous sections the metallicities are similar (within a few factor of each other), and the radiation fields are low in most of them. Therefore, it is possible that the invariability in the PAH spectra of the starburst in our sample is probably due to the similar conditions in these galaxies.

5.4. Molecular Hydrogen

We detect three pure-rotational transitions 0-0 S(2), S(1), and S(0) of H_2 at 12.28, 17.03, and 28.21 μm, respectively. The S(1) transition at 17.03 μm is the strongest of the three. Figure 14 shows that while there is some scatter, there is a good correlation of the H_2 lines with the [Si II] line. This is expected since both originate in the PDR. In fact, [Si II] is an important fine-structure cooling line of the PDR. We note that in order to combine the three lines we used a scaling factor between the SH and LH modules determined by matching the continuum in the overlap region in both modules around 19.5 μm. This is not ideal since no off observations were subtracted and it contributes to the scatter present in the figure. The ratio of the sum of the H_2 lines over the [Si II] line is 0.22, with values ranging from 0.04 to 0.5. This is very similar to the values found by Roussel et al. (2007) in their starburst (SINGS) sample.

The molecular hydrogen lines can be used to give information on the conditions of the warm component in the PDR. There is a relation between the density and temperature assuming local thermal equilibrium and using the Boltzman equation (van den Ancker et al. 2000; Bernard-Salas & Tielens 2005). Using this relation and the lines in the SH module (to avoid scaling effects), we have derived the excitation temperature (T_{ex}), column density $N(H_2)$, and warm molecular mass for the sample. These are given in Table 7. The average excitation temperature and column density are 360 $\pm$ 64 K and 2×10^{20} cm^{-2} respectively, and the warm molecular mass ranges from several 10^4 to $8\times10^6 M_\odot$, with an average mass of $1.1\times10^6 M_\odot$. We stress that these numbers correspond only to the region covered by the SH slit and are based on the fluxes for just the S(1) and S(2) lines.

Table 7
H_2 Conditions

Object	T_{ex}[a] (K)	$N(H_2)$ $\times10^{19}$ cm^{-2}	H_2 Mass $\times10^5 M_\odot$
NGC 253	523.7	49.9	0.2
NGC 520	282.5	22.7	10.1
NGC 660	358.9	29.1	2.2
NGC 1097	340.6	18.1	2.5
NGC 1222	277.1	21.0	10.8
NGC 1365	342.8	24.9	3.9
IC 342	492.5	9.2	0.1
NGC 1614	363.4	11.4	21.9
NGC 2146	343.2	35.2	4.7
NGC 2623	322.7	11.1	32.7
NGC 3079	378.2	45.9	7.0
NGC 3256	360.5	34.4	21.2
NGC 3556	298.6	5.3	0.5
NGC 3628	311.6	26.8	1.3
NGC 4088	372.6	5.5	0.5
NGC 4194	362.8	11.2	9.0
Mrk 52	472.9	1.5	0.7
NGC 4676	307.6	8.8	38.3
NGC 4818	292.2	32.4	1.4
NGC 4945	393.1	57.4	0.4
Mrk 266	326.6	12.5	82.4
NGC 7252	357.7	6.4	13.8
NGC 7714	399.5	4.6	3.3

Note.
[a] Based on the 0-0 S(1) and S(2) transitions.

Recently, Roussel et al. (2007) studied the warm molecular hydrogen emission in the nuclear region of a sample of SINGS galaxies. The range in areas covered in their observations (60 pc–3.8 kpc) is very similar to the range covered in our study (see Section 2). Their column densities compare well to those found for our starburst galaxies, but their excitation temperatures are on average cooler by ~150 K, and their masses are significantly larger (10^5–$10^8 M_\odot$). This is expected because the SINGS galaxies have a much lower star formation rate per unit volume compared to our starbursts, and since they are less luminous, a larger fraction of their molecular hydrogen is colder. "Cold" molecular hydrogen is traced by the S(0) line which is not used in our analysis as it falls in the LH slit, but it is used in the SINGS sample where the aperture size differences do not exist. Hence, our computed H_2 masses are lower than those found for the SINGS sample, but this is likely an artifact of the absence of the S(0) line in our calculations, rather than a real difference.

We find no relation between the excitation temperature and sources with and without AGNs. Higdon et al. (2006) analyzed *Spitzer* data of a sample of ULIRGs. Their average excitation temperature (336 $\pm$ 15 K) agrees with that of our starburst sample, but again their warm molecular masses are several hundreds times larger ($2\times10^8 M_\odot$). It is important to note that most ULIRGs fit in the SH aperture while in the starbursts we are only measuring the central region. Still, this difference may point as well to a larger fraction of mass being colder in the starburst sample.

6. CONCLUSIONS

1. We have presented high-resolution spectra ($R \sim 600$) of a sample (24) of nearby starburst galaxies. The spectra are

dominated by emission from forbidden fine-structure lines and PAH features.

2. [Ne V] is detected in six of the eight starbursts with a previously known AGN component. This line is also seen in NGC 4194.
3. Several PAH features have been measured in the spectra, some of which are weak and are rarely seen in the spectra of starburst galaxies and H II regions.
4. An emission feature around 10.7 μm and an absorption feature at 13.7 μm are detected for the first time. Their identification is unknown, but the strength of the feature at 10.7 μm correlates with that other PAH features.
5. The average conditions of the warm gas as traced by the S(1) and S(2) pure rotational molecular hydrogen lines indicate an average excitation temperature of 355 $\pm$ 60 K and a density of 2×10^{20} cm^{-2}. The warm molecular mass ranges from several 10^4 to $4\times10^6 M_\odot$.
6. We provide the combined average spectrum of the 15 "pure" starburst galaxies of our sample, which is likely the highest signal-to-noise mid-infrared spectrum of a $\sim 10^{11} L_\odot$ starburst galaxy available from the *Spitzer*. This template is representative of a large range in luminosity and IR color, and provides a good indication of the spectral properties of starburst galaxies at high redshift.

V.C. acknowledges partial support from the EU grants ToK 39965 and FP7-REGPOT 206469. We thank Ian Waters and Hongyu Xiao for their help with the line measurement.

REFERENCES

Allamandola, L. J., Tielens, A. G. G. M., & Barker, J. R. 1985, ApJ, 290, L25
Armus, L., et al. 2007, ApJ, 656, 148
Asplund, M., Grevesse, N., & Sauval, A. J. 2005, in Cosmic Abundances as Records of Stellar Evolution and Nucleosynthesis in Honor of David L. Lambert, ASP Conf. Ser., 336, ed. T. G. Barnes III & F. N. Bash (San Francisco, CA: ASP), 25
Asplund, M., Grevesse, N., & Sauval, A. J. 2006, Commun. Asteroseismol., 147, 76
Bernard-Salas, J., Pottasch, S. R., Beintema, D. A., & Wesselius, P. R. 2001, A&A, 367, 949
Bernard-Salas, J., Pottasch, S. R., Gutenkunst, S., Morris, P. W., & Houck, J. R. 2008, ApJ, 672, 274
Bernard-Salas, J., & Tielens, A. G. G. M. 2005, A&A, 431, 523
Blain, A. W., Smail, I., Ivison, R. J., Kneib, J.-P., & Frayer, D. T. 2002, Phys. Rep., 369, 111
Boulanger, F., Boissel, P., Cesarsky, D., & Ryter, C. 1998, A&A, 339, 194
Brandl, B. R., et al. 2006, ApJ, 653, 1129
Cohen, M., Megeath, T. G., Hammersley, P. L., Martin-Luis, F., & Stauffer, J. 2003, AJ, 125, 2645
Dale, D. A., et al. 2006, ApJ, 646, 161
Dale, D. A., et al. 2009, ApJ, 693, 1821
Dudik, R. P., et al. 2007, ApJ, 664, 71
Elbaz, D., & Cesarsky, C. J. 2003, Science, 300, 270
Farrah, D., et al. 2007, ApJ, 667, 149
Farrah, D., et al. 2008, ApJ, 677, 957
Feldman, U., & Widing, K. G. 2003, Space Sci. Rev., 107, 665
Förster Schreiber, N. M., Roussel, H., Sauvage, M., & Charmandaris, V. 2004, A&A, 419, 501
Galliano, F., Madden, S. C., Tielens, A. G. G. M., Peeters, E., & Jones, A. P. 2008, ApJ, 679, 310
Genzel, R., et al. 1998, ApJ, 498, 579
Gonzalez-Delgado, R. M., et al. 1995, ApJ, 439, 604
Grevesse, N., & Sauval, A. J. 1998, Space Sci. Rev., 85, 161
Groves, B., Nefs, B., & Brandl, B. R. 2008, MNRAS, 391, L113
Hao, L., et al. 2009, ApJ, in press
Henry, R. B. C., Kwitter, K. B., & Balick, B. 2004, AJ, 127, 2284
Higdon, S. J. U., Armus, L., Higdon, J. L., Soifer, B. T., & Spoon, H. W. W. 2006, ApJ, 648, 323
Higdon, S. J. U., et al. 2004, PASP, 116, 975
Ho, L. C., & Keto, E. 2007, ApJ, 658, 314
Hony, S., et al. 2001, A&A, 370, 1030
Houck, J. R., et al. 2004, ApJS, 154, 18
Hunter, D. A., & Kaufman, M. 2007, AJ, 134, 721
Kennicutt, R. C., Jr. 1998, ARA&A, 36, 189
Kessler, M. F., et al. 1996, A&A, 315, L27
Lagache, G., Puget, J.-L., & Dole, H. 2005, ARA&A, 43, 727
Laurent, O., et al. 2000, A&A, 359, 887
Le Floc'h, E., et al. 2005, ApJ, 632, 169
Lebouteiller, V., et al. 2008, ApJ, 680, 398
Leger, A., & Puget, J. L. 1984, A&A, 137, L5
Li, A., & Draine, B. T. 2001, ApJ, 554, 778
Lonsdale, C. J., Farrah, D., & Smith, H. E. 2006, Astrophysics Update 2, ed. J. W. Mason (Germany: Springer), 285
Lutz, D., et al. 2003, A&A, 409, 867
Marigo, P., Bernard-Salas, J., Pottasch, S. R., Tielens, A. G. G. M., & Wesselius, P. R. 2003, A&A, 409, 619
Martín-Hernández, N. L., et al. 2002, A&A, 381, 606
Neugebauer, G., et al. 1984, ApJ, 278, L1
Oliva, E., Moorwood, A. F. M., Drapatz, S., Lutz, D., & Sturm, E. 1999, A&A, 343, 943
Pastoriza, M. G., Dottori, H. A., Terlevich, E., Terlevich, R., & Diaz, A. I. 1993, MNRAS, 260, 177
Peeters, E., Spoon, H. W. W., & Tielens, A. G. G. M. 2004, ApJ, 613, 986
Peeters, E., et al. 2002, A&A, 390, 1089
Pilyugin, L. S., Contini, T., & Vílchez, J. M. 2004, A&A, 423, 427
Pottasch, S. R., & Bernard-Salas, J. 2006, A&A, 457, 189
Rigopoulou, D., et al. 1999, AJ, 118, 2625
Rosenberg, J. L., et al. 2008, ApJ, 674, 814
Roussel, H., Sauvage, M., Vigroux, L., & Bosma, A. 2001, A&A, 372, 427
Roussel, H., et al. 2007, ApJ, 669, 959
Rubin, R. H., et al. 2007, MNRAS, 377, 1407
Rubin, R. H., et al. 2008, MNRAS, 387, 45
Sloan, G. C., et al. 1999, ApJ, 513, L65
Smith, J. D. T., et al. 2007, ApJ, 656, 770
Spoon, H. W. W., et al. 2007, ApJ, 654, L49
Stasinska, G. 1990, A&AS, 83, 501
Sturm, E., et al. 2002, A&A, 393, 821
Thornley, M. D., et al. 2000, ApJ, 539, 641
van den Ancker, M. E., Tielens, A. G. G. M., & Wesselius, P. R. 2000, A&A, 358, 1035
Van Kerckhoven, C., et al. 2000, A&A, 357, 1013
Verma, A., et al. 2003, A&A, 403, 829
Vermeij, R., & van der Hulst, J. M. 2002, A&A, 391, 1081
Wang, W., & Liu, X.-W. 2008, MNRAS, 389, 33
Weedman, D. W., et al. 1981, ApJ, 248, 105
Weedman, D. W., et al. 2005, ApJ, 633, 706
Werner, M., et al. 2004, ApJS, 154, 1
Wu, Y., Charmandaris, V., Hao, L., Brandl, B. R., Bernard-Salas, J., Spoon, H. W. W., & Houck, J. R. 2006, ApJ, 639, 157
Wu, Y., et al. 2008, ApJ, 673, 193